ACS EARTH AND SPACE CHEMISTRY

http://pubs.acs.org/journal/aesccq

Article

HCOOH in the Remote Atmosphere: Constraints from Atmospheric Tomography (ATom) Airborne Observations

Xin Chen, Dylan B. Millet,* J. Andrew Neuman, Patrick R. Veres, Eric A. Ray, Róisín Commane, Bruce C. Daube, Kathryn McKain, Joshua P. Schwarz, Joseph M. Katich, Karl D. Froyd, Gregory P. Schill, Michelle J. Kim, John D. Crounse, Hannah M. Allen, Eric C. Apel, Rebecca S. Hornbrook, Donald R. Blake, Benjamin A. Nault, Pedro Campuzano-Jost, Jose L. Jimenez, and Jack E. Dibb

Cite This: *ACS Earth Space Chem.* 2021, 5, 1436−1454

Read Online

ACCESS | Metrics & More | Article Recommendations | Supporting Information

ABSTRACT: Formic acid (HCOOH) is an important component of atmospheric acidity but its budget is poorly understood, with prior observations implying substantial missing sources. Here, we combine pole-to-pole airborne observations from the Atmospheric Tomography Mission (ATom) with a chemical transport model (GEOS-Chem CTM) and back-trajectory analyses to provide the first global in situ characterization of HCOOH in the remote atmosphere. ATom reveals sub-100 ppt HCOOH concentrations over most of the remote oceans, punctuated by large enhancements associated with continental outflow. Enhancements correlate with known combustion tracers and trajectory-based fire influences. The GEOS-Chem model underpredicts these in-plume HCOOH enhancements, but elsewhere, we find no broad indication of a missing HCOOH source in the background free troposphere. We conclude that missing nonfire HCOOH precursors inferred previously are predominantly short-lived. We find indications of a wet scavenging underestimate in the model consistent with a positive HCOOH bias in the tropical upper troposphere. Observations reveal episodic evidence of ocean HCOOH uptake, which is well-captured by GEOS-Chem; however, despite its strong seawater undersaturation, HCOOH is not consistently depleted in the remote marine boundary layer. Over 50 fire and mixed plumes were intercepted during ATom with widely varying transit times and source regions. HCOOH:CO-normalized excess mixing ratios in these plumes range from 3.4 to >50 ppt/ppb CO and are often over an order of magnitude higher than expected primary emission ratios. HCOOH is thus a major reactive organic carbon reservoir in the aged plumes sampled during ATom, implying important missing pathways for in-plume HCOOH production.

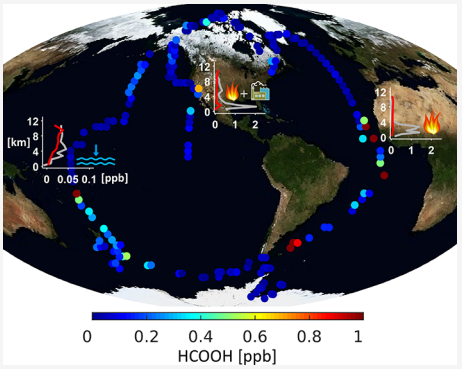

KEYWORDS: *formic acid, remote atmosphere, fire, deposition, Atmospheric Tomography Mission, iodide CIMS, chemical transport model, back trajectory*

1. INTRODUCTION

Formic acid (HCOOH) is ubiquitous in the atmosphere, one of the largest drivers of precipitation acidity in remote regions,[1−3] and a major OH sink in the aqueous phase.[4] HCOOH therefore acts as a pH buffer and affects aqueous phase chemistry through its effects on oxidant levels, pH-dependent reaction rates, and solubilities. Prior work has shown HCOOH to be present in the atmosphere at levels far greater than can be explained based on its known sources and sinks;[5−8] however, such studies have mainly focused on terrestrial and near-source regions. Here, we combine observations from the NASA DC-8 flying laboratory during the Atmospheric Tomography Mission (ATom-3 and ATom-4) with a global chemical transport model (GEOS-Chem CTM) to provide the first global in situ characterization of HCOOH in the remote atmosphere.

Recent evaluations of the global HCOOH budget have estimated its total known source at ∼60 Tg/year with subsequent removal dominated by deposition.[5,6] Photochemical production from volatile organic compounds (VOCs) is believed to be the dominant HCOOH source over forested regions,[9,10] urban areas,[11] and on a global scale,[5,6] with direct emissions from the terrestrial biosphere,[12] soils,[13] ants,[14] and urban/industrial activities[15] playing more modest roles. Secondary formation pathways that have been identified include hydroxyl radical (OH)- and ozone (O_3)-initiated

Received: February 17, 2021
Revised: April 29, 2021
Accepted: April 30, 2021
Published: May 13, 2021

https://doi.org/10.1021/acsearthspacechem.1c00049
ACS Earth Space Chem. 2021, 5, 1436−1454

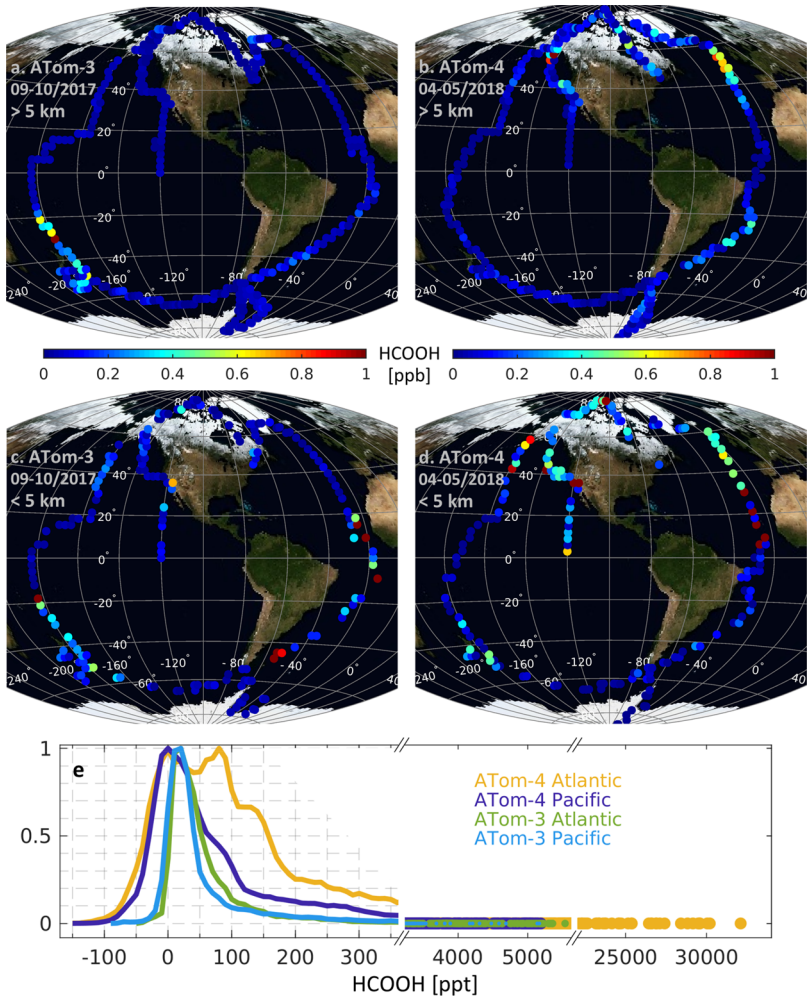

Figure 1. Observed HCOOH distribution during ATom-3 and ATom-4. Panels (a) and (c) map the HCOOH mixing ratios measured during ATom-3 above (a) and below (c) 5 km altitude. Panels (b) and (d) show the corresponding plots for ATom-4. Each datapoint in panels (a)−(d) is colored by the mean HCOOH mixing ratio for the surrounding 1.5° latitude × 1.5° longitude bin. Panel (e) shows normalized frequency distributions for the ATom HCOOH observations with different linear scales at the upper range of the distribution. Some negative values occur reflecting uncertainty and variability in the instrument background signal.

oxidation of isoprene, monoterpenes, and their oxidation products,[16] ozonolysis of other alkenes,[17] and alkyne oxidation.[18] Acetaldehyde has also been shown to be a precursor of HCOOH via its phototautomerization to vinyl alcohol;[19] subsequent work using the GEOS-Chem CTM found that this pathway can account for up to 60% of the modeled HCOOH production over remote oceans.[20] Aerosol aging has been implicated as another HCOOH source through heterogeneous (or condensed-phase) oxidation by OH,[21] ozonolysis,[22] and photolysis.[23−26]

HCOOH is also produced from biomass burning,[27−30] and recent work indicates that this source may be larger than previously thought. Yokelson et al.[31] found that in many biomass burning plumes organic acids are the third most important carbon reservoir—behind CO_2 and CO and ahead of CH_4. The same authors reported organic acid:CO enhancement ratios of up to 18% (mol/mol) in aged fire plumes—with secondary acid production exceeding the abundance of known precursors—and invoked unmeasured pyrogenic VOCs as explanation. Chaliyakunnel et al.,[32] Pommier et al.,[33] and Yamanouchi et al.[34] likewise observed fire HCOOH:CO enhancement ratios much higher than primary emission ratios could explain, implying substantial HCOOH production during fire plume aging.

High levels of HCOOH have also been measured in remote areas, with a variety of formation mechanisms proposed. For example, Baboukas et al.[35] argued that an indirect marine HCOOH source of ∼50 Tg/year globally was required to explain measured mixing ratios (averaging ∼450 ppt) in the Atlantic marine boundary layer (MBL). Dibb and Arsenault[36] measured higher HCOOH in firn air (up to 6 ppb) than in the overlying atmosphere and invoked a source from the oxidation of organics in snow. Dibb et al.[37] presented strong evidence of enhanced formic acid at Summit, Greenland, from the long-range transport of wildfire smoke. Jones et al.[38] measured HCOOH concentrations in the European Arctic MBL that were 50% higher than over the surrounding land areas, and they proposed a source from stabilized Criegee intermediates following photolysis of ocean-released diiodomethane (CH_2I_2). Mungall et al.[39] reported HCOOH levels of up to 4 ppb in the Canadian Arctic MBL, with evidence pointing to a photochemical or heterogeneous source from the sea surface microlayer.

The above findings highlight the need for a better understanding of atmospheric HCOOH and its sources and

https://doi.org/10.1021/acsearthspacechem.1c00049
ACS Earth Space Chem. 2021, 5, 1436−1454

sinks. A key open question is whether the inferred missing HCOOH source persists throughout the global atmosphere (for example, as inferred for acetaldehyde in Wang et al.[40]), which would imply a ubiquitous long-lived precursor pool, or if it primarily manifests near and downwind of continental VOC source regions. The ATom campaign[41] collected observations of HCOOH and a suite of related tracers from pole-to-pole over the remote Pacific and Atlantic Oceans with continuous vertical profiling and across multiple seasons (Figure 1). The dataset thus provides a new opportunity to address the above science issues on a global scale. In this paper, we apply the GEOS-Chem CTM to interpret the ATom measurements in terms of their implications for the HCOOH budget in the remote atmosphere.

2. METHODS

2.1. Atmospheric Tomography (ATom) 3 and 4 Aircraft Campaigns. HCOOH measurements were conducted onboard a NASA DC-8 aircraft as part of the two final ATom deployments[41] in September−October 2017 (ATom-3) and April−May 2018 (ATom-4). ATom was designed to (i) perform detailed chemical characterization of the global remote atmosphere, (ii) establish a comprehensive dataset of climatically and chemically important atmospheric constituents, and (iii) provide new observations to improve models.[42] Each ATom deployment spans nearly pole-to-pole over the Pacific and Atlantic Oceans with continuous vertical profiling from within the MBL to above the tropopause.

2.1.1. HCOOH Measurements by Iodide-Ion Time-of-Flight Chemical Ionization Mass Spectrometry (I-CIMS) during ATom-3 and ATom-4. HCOOH was measured once per second using an iodide-ion time-of-flight chemical ionization mass spectrometer (I-CIMS), as described by Veres et al.[43] Pressure and temperature control of the sampling inlet and humidity control of the ion-molecule reaction region guaranteed that the instrument response was independent of aircraft altitude and ambient conditions. The 70 cm long Teflon inlet tube was controlled to 40 °C and at ambient pressure. The pressure upstream of the ion-molecule reaction region was controlled to 140 mb, and the ion-molecule reaction region itself was controlled to 40 mb (ATom-4) or 50 mb (ATom-3) to maintain constant ion-molecule reaction times. The measurement sensitivity to HCOOH depends on the water concentration in the ion-molecule reaction region, and water vapor was added to this region to compensate for changing ambient humidity and maintain constant detection sensitivity. The ratio of the two reagent ions (iodide and the iodide-water cluster) served as a proxy for humidity in the instrument, and water was controlled to maintain a constant reagent-ion cluster ratio. Effects of any residual humidity changes were then corrected based on a laboratory quantification of the water-dependent HCOOH sensitivity as a linear function of the iodide:iodide-water ion ratio.

HCOOH was detected as a cluster with iodide at m/z 172.9105, with a resolution of $m/\Delta m$ = 5000. The instrument sensitivity to HCOOH was determined before and after the campaign by a laboratory-based standard addition of HCOOH from a permeation tube source with the instrument in its flight configuration. The permeation tube was held in an oven controlled to 40 °C with a 50 sccm continuous flow of N_2. The HCOOH emission from the permeation tube was determined by catalytically converting HCOOH to CO_2 followed by CO_2 detection.[44] The 47 ng/min HCOOH permeation tube emission was mixed with the 6 slm inlet flow to give a 3.8 ppb calibration mixing ratio. The uncertainty in this calibration process is approximately 15%. Under typical operating conditions, the instrument sensitivity was approximately 8 ion counts/s/ppt HCOOH, with reagent ion signals of 3 MHz for iodide and 1.5 MHz for the iodide-water cluster. In-flight calibrations of chlorine and nitric acid demonstrated that the reagent-ion-normalized instrument sensitivity did not change over the course of each campaign.

The instrument zeros were determined in-flight for 30 s every 8 min by overfilling the inlet with ambient air drawn through a scrubber. After ATom-4, an additional background measurement capability was added that involved the periodic addition of dry N_2 at the inlet tip without going through a scrubber. These two zeroing methods were found to agree to within the variability of the background determinations. For ATom, average background signals were typically 300 ppt; these were interpolated between consecutive determinations and subtracted from the total signal to determine the ambient HCOOH contribution. Background signals varied by 50 to 100 ppt between successive quantifications, imposing an additional 50−100 ppt measurement uncertainty (and a lower limit of detection, LOD) that is not reduced by averaging over times less than background measurement interval. The measurement precision was better than the instrument background uncertainty, and was typically below 10 ppt for 1 s measurements, ranging from 3 to 15 ppt.

2.1.2. Other Measurements. The DC-8 aircraft featured a large instrument payload during ATom, and we employ the following measurements to aid interpretation of the HCOOH dataset. For species measured by more than one instrument, dataset selection was based on time response, data availability, and nominal accuracy. Carbon monoxide (CO) was measured with the NOAA Picarro cavity ring-down spectrometer (G2401-m)[45] and with the Harvard quantum cascade laser system (QCLS).[46] We use here the merged CO.X product,[41] which is based primarily on the QCLS observations with gaps filled using the NOAA Picarro observations. We employ hydrogen cyanide (HCN) observations from the Caltech chemical ionization mass spectrometer using CF_3O^- reagent ions (CIT-CIMS)[47,48] and formaldehyde (HCHO) observations from the NASA in situ airborne formaldehyde (ISAF) instrument.[49,50] Other VOC measurements used here were performed with the NCAR trace organic gas analyzer (TOGA)[51] and the UC-Irvine whole air sampling system (WAS).[52] NO_x ($NO + NO_2$) was measured by the NOAA nitrogen oxides and ozone (NO_yO_3) instrument.[53] Black carbon (BC) was measured with the NOAA single-particle soot photometer (SP2).[54] Submicron organic aerosol (OA) was measured with the University of Colorado high-resolution time-of-flight aerosol mass spectrometer (HR-AMS).[55,56] BC and OA are both reported for T = 273 K and P = 1013 hPa; we performed all unit conversions accordingly. Submicron organic carbon aerosol (OC) was derived from OA based on the OA:OC ratio reported by the instrument team. We use the particle analysis by laser mass spectrometry (PALMS) biomass burning particle number fraction[57] in our analysis to aid in plume source attribution. Finally, we use the cloud indicator values from the cloud, aerosol, and precipitation spectrometer (CAPS)[58] to identify within-cloud sampling periods.

2.2. GEOS-Chem Simulation. We use the GEOS-Chem CTM in its classic mode,[59] with detailed HO_x-NO_x-VOC-ozone-halogen-aerosol chemistry following JPL/IUPAC rec-

https://doi.org/10.1021/acsearthspacechem.1c00049
ACS Earth Space Chem. 2021, 5, 1436−1454

ommendations and photolysis frequencies calculated using Fast-JX algorithms.[60−62] The simulation is driven by assimilated meteorological data (Goddard Earth Observation System Forward Processing, GEOS-FP) from the NASA Global Modeling and Assimilation Office (GMAO) and conducted at 2° × 2.5° horizontal resolution with time steps of 15 min (transport/convection) and 30 min (chemistry/emission). We use the TPCORE advection algorithm,[63] convective mass fluxes from the meteorological archive,[64] and nonlocal boundary layer mixing.[65]

We employ a customized GEOS-Chem simulation for HCOOH building on prior work by Shaw et al.,[20] Millet et al.,[5] and Paulot et al.[6] Photochemical HCOOH production proceeds as described by Millet et al., with phototautomerization of acetaldehyde updated according to Shaw et al.[20] Global anthropogenic emissions for HCOOH and other species are from the Community Emissions Data System inventory,[66] overwritten for Africa by the Diffuse and Inefficient Combustion Emissions in Africa dataset (DICE-Africa).[67] Global HCOOH emissions from agriculture and natural soils are scaled to the corresponding ammonia and NO_x fluxes following prior work.[6] Direct HCOOH biogenic emissions are calculated using the Model of Emissions of Gases and Aerosols from Nature version 2.1 (MEGAN v2.1),[68] implemented in GEOS-Chem as described by Hu et al.[69] Biomass burning emissions are based on the Global Fire Emissions Database with small fires (GFED4s)[70] with recommended species-specific emission factors (http://www.globalfiredata.org).[71] Ocean emissions of HCOOH precursors (alkenes and isoprene) are estimated following Millet et al.[5] and Paulot et al.[6] Dry deposition of HCOOH and other species is computed using a modified Wesely scheme;[72,73] over oceans, this is equivalent to an infinite liquid-phase sink and hence unidirectional air-to-sea flux. The resulting monthly mean HCOOH dry deposition velocities during the timeframes of ATom-3 and ATom-4 typically range between near-zero and 0.8 cm/s over land and reach 2.2 cm/s over ocean. Wet deposition is as described by Amos et al.[74] and Mari et al.[75] Uptake of HCOOH on ice and dust follows Paulot et al.[6]

2.3. Back-Trajectory Analysis. We use atmospheric back trajectories computed along the ATom flight tracks with the Traj3D model[76,77] to interpret the observations in terms of their source footprint and source/sink influences. The model is driven by National Centers for Environmental Prediction (NCEP) Global Forecast System (GFS) 0.5° × 0.5° resolution meteorology. For each minute along the flight track, a cluster of 245 trajectories is initialized in a 0.3° latitude × 0.3° longitude × 20 hPa cube centered on the aircraft position. Each trajectory is then run 30 days backward with a 3 h time-step. Traj3D model results used here include individual trajectories, cluster ensemble distributions, and cluster-average results.

Two influence processes are employed in this work, as follows. (1) Fire influence: a trajectory is considered fire-influenced if it encountered a fire hotspot at a time and location indicated by one of the following three products: moderate-resolution imaging spectroradiometer (MODIS) fire radiative power (FRP) (collection 6);[78] visible infrared imaging radiometer suite (VIIRS) 375-m FRP;[79] or Global Fire Emissions Database (GFED) v2. Fire plume heights were calculated based on FRP for MODIS and VIIRS and assumed to be within the boundary layer for GFED. (2) Land boundary layer (BL): a trajectory is considered to be influenced by the land boundary layer if it entered the BL over any continent.

3. RESULTS AND DISCUSSION

3.1. HCOOH Distribution over Remote Oceans and the Role of Fire Plumes in Driving Variability. Figure 1 shows horizontal and frequency distributions of HCOOH mixing ratios observed during ATom-3 and ATom-4. We see that the ATom flights sampled a broad range of HCOOH concentrations from below the instrumental LOD to above 30 ppb (Figure 1e). However, the majority of the distribution is characterized by very low concentrations, with 80% (ATom-3) and 61% (ATom-4) of the data falling below 100 ppt (Figure 1). While the instrumental LOD prevents accurate quantification of the lowest observed concentrations, the data clearly reveal sub-100 ppt HCOOH background concentrations over most of the remote oceans. More frequent HCOOH enhancements are apparent during ATom-4 than ATom-3 (Figure 1e); as will be seen, this reflects strong fire influence during this campaign. In general, lower HCOOH mixing ratios are seen aloft (Figure 1a,b vs Figure 1c,d) but with clear enhancements in certain regions: east of Australia, east of South America, and over the springtime northern oceans.

Figure 2a compares the vertical HCOOH distribution observed during ATom to that seen in prior aircraft campaigns

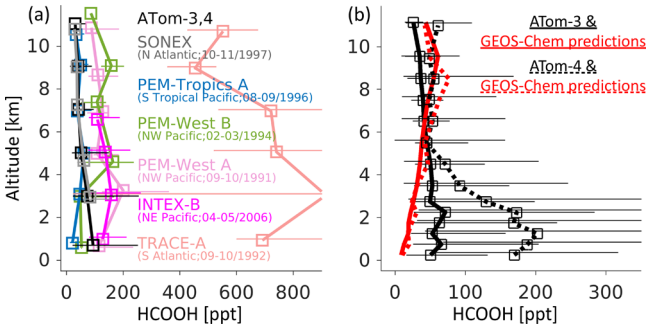

Figure 2. Median HCOOH vertical profiles measured during ATom-3 and ATom-4, and comparison with (a) prior aircraft observations over ocean and (b) GEOS-Chem model predictions. The vertical bin resolution differs between panels (a) and (b) (a: 2 km; b: 0.5 km below 3 km altitude, 1 km above 3 km altitude) to reflect differing sampling densities between the campaigns. Horizontal bars indicate 25th−75th percentiles for each vertical bin. For panel (a), observations over land have been filtered out, and the SONEX dataset further employs ozone and latitude filters following Singh et al.[134] See Table S1 for details on the aircraft campaigns plotted in panel (a).

(Table S1) over the ocean. We see that the median ATom HCOOH profile is very similar to that observed during SONEX (10−11/1997)[80] and PEM-Tropics A (08−09/1996),[81] particularly in the free troposphere. PEM-West A (09−10/1991),[82] PEM-West B (02−03/1994),[83] and INTEX-B (04−05/2006)[84,85] sampled closer to land, with the associated Asian/North American outflow leading to higher median HCOOH concentrations. TRACE-A (09−10/1992)[86] encountered extremely high HCOOH levels in the south Atlantic due to biomass burning in South America and southern Africa. Together, these campaigns are consistent in revealing HCOOH concentrations on the order of <100 ppt over the remote oceans, rising to >100 ppt closer to

https://doi.org/10.1021/acsearthspacechem.1c00049
ACS Earth Space Chem. 2021, 5, 1436−1454

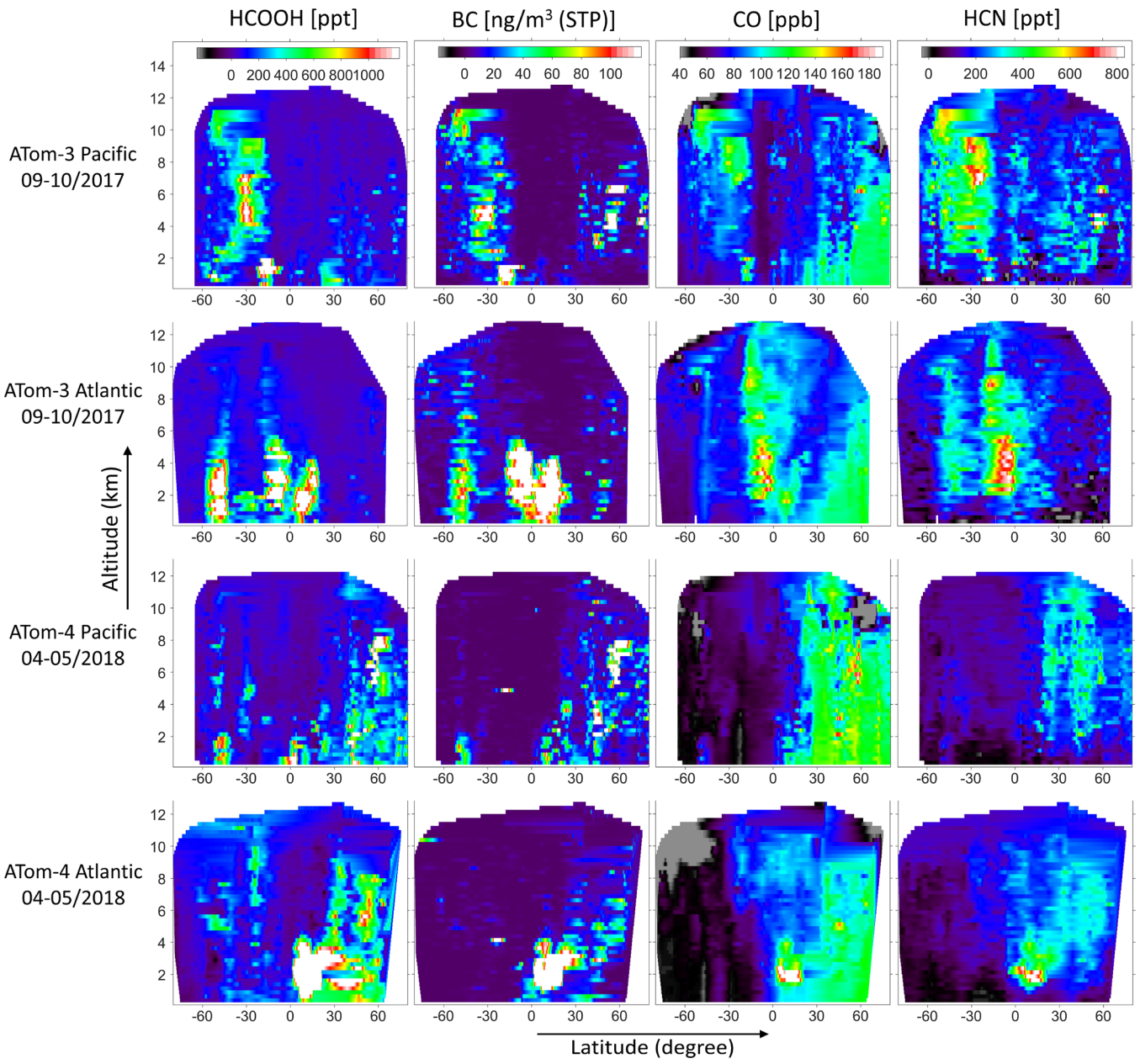

Figure 3. Interpolated tracer latitude−altitude cross sections based on ATom-3 (Northern Hemisphere fall) and ATom-4 (Northern Hemisphere spring) in situ observations. 1 Hz data are gridded and interpolated into 0.05° latitude × 250 m altitude bins.

continental regions, and much higher under strong fire influence.

Figure 2b compares the ATom-3 and ATom-4 vertical HCOOH profiles with those simulated by GEOS-Chem. For both campaigns, the model significantly underestimates the median-observed concentrations in the lower atmosphere, with the discrepancy more severe during ATom-4. On the other hand, the model captures the median HCOOH concentrations seen in the mid-to-upper free troposphere with no appreciable bias. This contrasting behavior will be further discussed in Section 3.2.

Figure 3 compares interpolated (0.05° latitude × 250 m) latitude−altitude curtains for HCOOH, CO, BC, and HCN based on the ATom-3 and ATom-4 observations. While CO exhibits a clear latitudinal gradient with elevated concentrations throughout the northern high latitudes, no consistent gradient is detectable for HCOOH. Instead, we observe persistently low (<100 ppt) background HCOOH concentrations throughout most of the remote atmosphere with discrete enhancements at specific locations associated with terrestrial outflow. The strongest such enhancements occur during spring (Southern Hemisphere for ATom-3; Northern Hemisphere for ATom-4) and consistently over the tropical Atlantic (Figure 3). This pattern is very similar to that seen for BC, a known combustion tracer. In fact, the HCOOH correlation with BC is higher than with any other ATom-measured species (R = 0.72 and 0.74 for the entire ATom-3 and ATom-4 datasets, respectively; flight-specific values reach 0.86; Figure S1). The localized nature of the strongest enhancements, their locations and their distances from population centers, together points to a predominant role for biomass burning in driving remote HCOOH variability.

BC is also emitted from other forms of combustion, and the Figure 3 enhancements presumably also include some

https://doi.org/10.1021/acsearthspacechem.1c00049
ACS Earth Space Chem. 2021, 5, 1436−1454

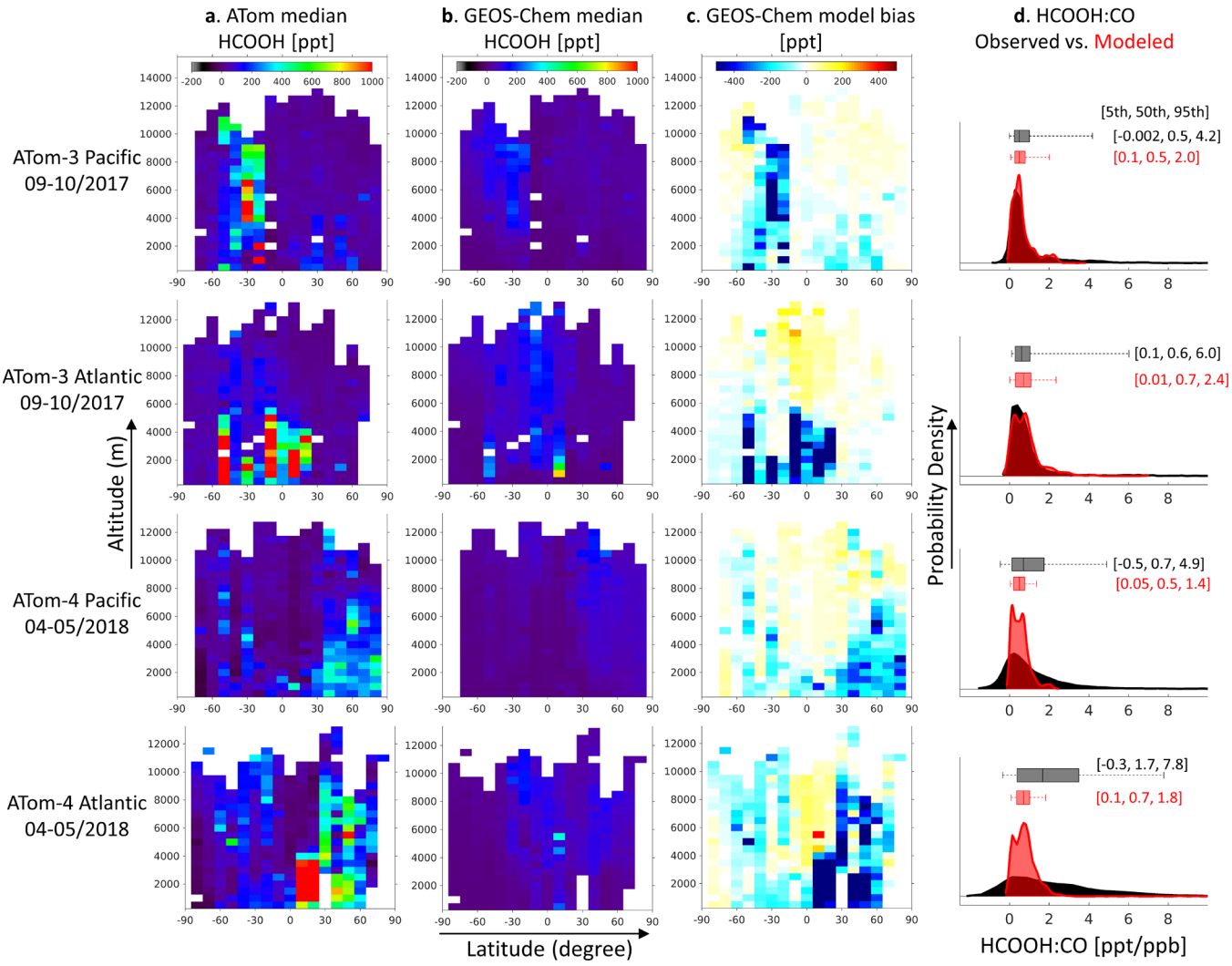

Figure 4. (a)−(c) Median gridded (10° latitude × 500 m altitude) HCOOH cross sections. Plotted are the (a) ATom observations, (b) GEOS-Chem model predictions, and (c) absolute model bias. Column (d) shows kernel-smoothed probability density distributions and box-whisker plots (5th−25th−50th−75th−95th percentiles) for the HCOOH:CO ratio as measured during ATom (black) and modeled by GEOS-Chem (red) with numbers inset representing (left to right) the 5th, 50th, and 95th percentiles of the distribution.

contributions from nonfire sources such as urban pollution. Notably, the HCOOH correlation with HCN (a biomass burning tracer) is not as high as with BC (Figure S1); this may reflect the large variability in fire HCN emissions[87] and the differing removal pathways for HCN and HCOOH. Overall, the strong importance of fires for HCOOH is confirmed by its tight correlation with the trajectory-derived fire influence (Figure S2)—HCOOH enhancements under recent fire influence are an order of magnitude higher than under general land boundary layer influence. Later (Section 3.4), we will assess the importance of primary emissions versus in-plume production in driving these HCOOH enhancements and explore the role of HCOOH as a reactive carbon reservoir in highly aged fire plumes.

Despite the high overall HCOOH-BC correlation, we see in Figure 3 instances where their spatial patterns differ. For example, elevated HCOOH is observed in the MBL at ∼30° N over the Pacific during ATom-3 with no accompanying BC enhancement. Also during ATom-3, comparable HCOOH enhancements are seen over the tropical and southern Atlantic, whereas for BC the tropical enhancements are far more pronounced. Such differences can arise from factors such as secondary production of HCOOH, nonpyrogenic sources, and differing removal rates.

The following sections combine the ATom observations with GEOS-Chem model predictions to (i) evaluate current model treatment of HCOOH in the remote marine atmosphere (outside of fire plumes) in terms of evidence for broad-scale missing sources and (ii) diagnose signatures of HCOOH removal and the degree to which these are captured in the GEOS-Chem simulation. We return to examine the role of fires for remote HCOOH in Section 3.4.

3.2. Is there a Ubiquitous Missing HCOOH Source in the Background Free Troposphere? Several prior studies have demonstrated the existence of large missing HCOOH sources,[5−8,16,39] which is consistent with the model-measurement discrepancies seen during ATom in the lower troposphere (Figure 2b). On the other hand, Figure 2b shows that for both ATom-3 and ATom-4, GEOS-Chem is able to capture the median observed HCOOH abundance in the free troposphere with no detectable low bias. Median model levels in the free troposphere are generally in the 50−100 ppt range; if there were persistent missing sources leading to concentrations significantly >100 ppt, they would be detectable given

https://doi.org/10.1021/acsearthspacechem.1c00049
ACS Earth Space Chem. 2021, 5, 1436−1454

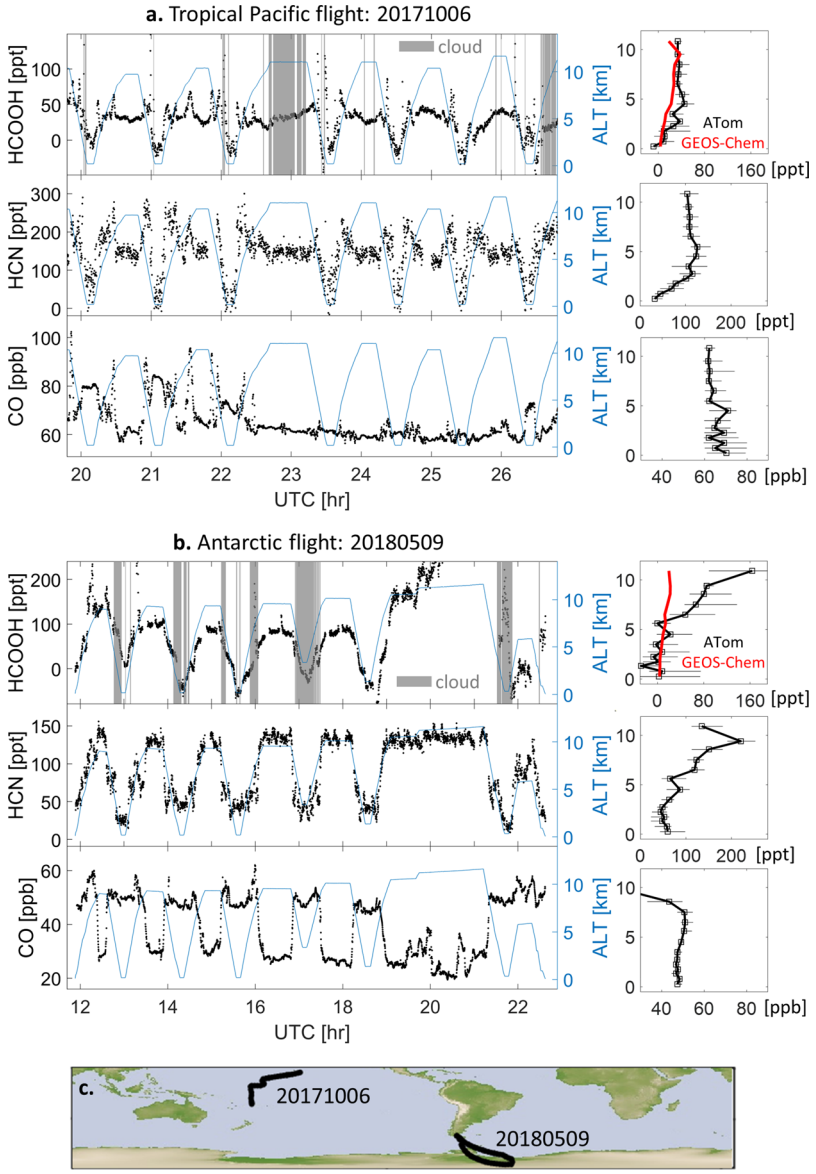

Figure 5. Ocean uptake of HCOOH as evident during two background flights: (a) a tropical Pacific flight on 10/06/2017 and (b) an Antarctic flight on 05/09/2018. Left panels show the time series for three trace gases (black) and altitude (blue). Shaded regions (gray) in the HCOOH panel indicate cloudy conditions (liquid-phase, mixed-phase, or cirrus clouds) based on CAPS observations. Right panels show the corresponding median observed vertical profiles for the entire flight (in black) with horizontal bars denoting the 25th−75th percentiles. The observed HCOOH profile is compared to GEOS-Chem model predictions (in red). Panel (c) shows the two flight tracks (black).

the instrumental LOD. Strong model HCOOH underestimates are seen in the vicinity of plumes and in the springtime northern latitudes but do not occur ubiquitously across the remote free troposphere (Figure 4) or at any altitude when >10 days removed from any land boundary layer or fire influence (Figure S2). In fact, there is some indication of a positive model bias in the free troposphere (e.g., at high altitudes over the tropical Atlantic; Figure 4), which we will discuss further in Section 3.3.

The comparisons above imply that the large missing sources of HCOOH inferred in prior work are mainly terrestrial and sufficiently short-lived that their effects do not manifest as a consistent detectable model bias in the ATom dataset. Figure S3 shows that median levels for key measured HCOOH precursors are indeed very low during ATom, and this is generally captured by the model (although with underestimates for ethyne and acetaldehyde). We likewise conclude that the fire plume enhancements discussed earlier do not reflect a source of sufficient global magnitude to yield a detectable model HCOOH bias throughout the remote atmosphere.

Recent ATom-based analyses by Wang et al.[40] and Travis et al.[88] point to a widespread missing acetaldehyde source in the free troposphere over remote oceans, which is also seen here (Figure S3). Unidentified precursor VOCs are one possible explanation; if so, it appears that those VOCs do not give rise to large amounts of HCOOH. In addition, while acetaldehyde itself is a HCOOH precursor via tautomerization to vinyl alcohol,[19,89−92] we find that the model bias for this species is insufficient to have a large broad-scale impact on HCOOH. Specifically, a sensitivity simulation doubling the vinyl alcohol source from acetaldehyde yields a modeled HCOOH increase of <1 ppt over most remote areas. Thus, while acetaldehyde tautomerization can be a large fraction of the total modeled

https://doi.org/10.1021/acsearthspacechem.1c00049
ACS Earth Space Chem. 2021, 5, 1436−1454

HCOOH production rate in remote areas,[20] the absolute production rate is quite small in such cases.

3.3. Air−Sea Exchange and Wet Scavenging of HCOOH. HCOOH has a high gas-to-aqueous partitioning tendency with an intrinsic Henry's law constant of k_H = 8917 M/atm at 298K.[93−95] Its aqueous uptake is further enhanced by dissociation (pK_a = 3.75) in natural solvents such as rainwater (pH ∼5.6; $k_H^{eff} = 6 \times 10^5$ M/atm at T = 298 K) and ocean water (pH ∼8.1; $k_H^{eff} = 2 \times 10^8$ M/atm at T = 298 K). As a result, wet scavenging is thought to be the dominant global sink of atmospheric HCOOH,[6] and the signature of this process is indeed evident in the ATom dataset. For example, HCN and CO co-enhancements in the tropical Atlantic upper troposphere (Figure 3) indicate the presence of transported fire plumes. However, no comparably strong HCOOH or BC enhancements are apparent in the same locations, implying wet removal of these species by convective updrafts, clouds, or precipitation during plume transport. The differing behavior for HCOOH versus HCN can be explained by the much weaker solubility (k_H = 12 M/atm at 298 K[93]) and acid dissociation (pK_a = 9.2) for HCN. In the GEOS-Chem simulation, we thus derive a global HCOOH lifetime of ∼8 days against wet deposition, whereas this is a negligible removal pathway for HCN.[96,97] The fact that the model frequently overestimates HCOOH at high altitudes, particularly over the tropical Atlantic (Figure 4, Section 3.2), may reflect an underestimate of convective HCOOH removal—as has been identified previously in the model for black carbon and sea salt aerosols.[98]

The ATom data also include segments with clear evidence of oceanic HCOOH uptake. Figure 5 shows measurements of HCOOH and related tracers during two flights with a minimal continental influence (based on CO, BC, and HCN, not all shown) over the Tropical Pacific and Antarctic Oceans. We see strong HCOOH depletion in the MBL for nearly all of the vertical profiling maneuvers (others are apparently influenced by fire or pollution plumes). HCN is likewise depleted in the MBL, whereas CO is enhanced. MBL depletion of HCOOH could in theory be explained either by cloud scavenging or by ocean uptake. However, the time series in Figure 5 shows that MBL depletion of HCOOH is not dependent on cloudy conditions—arguing against cloud scavenging as the major driver. Similar HCOOH depletion in the MBL was previously observed during an airborne ascent/descent over the European Arctic Ocean.[38]

Figure 5 also compares the HCOOH vertical profiles from the above remote flights with model predictions, showing that GEOS-Chem generally reproduces the observed 0−5 km vertical gradient. While the observations have high relative uncertainty at these low concentrations, this agreement supports the idea that an air-side resistance-in-series deposition mechanism can adequately represent ocean HCOOH uptake without considering its degree of saturation or liquid-side resistance. For example, based on the effective Henry's constant above, 1 ppb and 1 ppt of atmospheric HCOOH correspond at equilibrium to surface ocean [$HCOOH_{(aq)}$ + $HCOO^-$] concentrations of 0.2 M and 0.2 mM, respectively (and higher at lower temperatures), with formate as the predominant dissolved form ([$HCOOH_{(aq)}$]:[$HCOO^-$] = 4.5 × 10^{-5} at pH = 8.1). With very few exceptions,[99] literature-reported seawater formate concentrations are in the μM or nM range (Table S2[100−104])—orders of magnitude below the saturation concentration. It is clear therefore that the oceans are strongly undersaturated for HCOOH and that the bulk ocean−atmosphere flux should be effectively unidirectional. In this way, we find in GEOS-Chem that ocean uptake accounts for 14% of the global annual HCOOH removal through dry deposition, corresponding to 5% of the total sink (Table S3).

However, the MBL depletion of HCOOH discussed above is not consistently present across all of the ATom flights and profiles. In particular, the mean ATom-3 and ATom-4 latitude−altitude cross sections (Figure 3) show consistent MBL depletion for HCN but not for HCOOH. Based on solubility alone, we would conversely expect a stronger uptake signal for HCOOH than for HCN; the lack of a consistent HCOOH ocean uptake signature in the ATom observations implies that other processes are obscuring that signal. For example, Figure S4 shows a series of ATom vertical profiles in which HCN is characteristically depleted in the MBL but HCOOH is strongly enhanced. BC and CO co-enhancements for these same profiles suggest a fire and/or pollution influence. However, given their expected co-emission and solubility difference, it is then surprising that HCN would be scrubbed from the plume while the HCOOH enhancement persists. This may reflect ongoing secondary production during plume transport or a marine boundary layer source of uncertain mechanism.[38,39]

3.4. Large and Variable HCOOH Sources from Fires. We have seen above that fire plumes are key drivers of HCOOH variability in the remote atmosphere sampled by ATom. This influence is strongly underestimated by GEOS-Chem. Figure 4 plots the latitude−altitude HCOOH curtains from Figure 3 as median values over 10° latitude × 500 m altitude bins for comparison with the model. The enhancement patterns visible in Figure 3 still emerge in the median values and at the coarser spatial resolution of Figure 4. While the model exhibits some fidelity in the simulated enhancement locations, predicted magnitudes are far weaker than observed. This tendency is also seen in the HCOOH:CO concentration ratios: Figure 4 shows that during ATom-3 and the Pacific leg of ATom-4, the model captures the central part of the HCOOH:CO distribution but misses the upper tail. A larger model bias is evident over the Atlantic during ATom-4, where the model underestimates the median HCOOH:CO ratio by a factor of >2 and the 95th percentile by a factor of >4.

We proceed to examine these HCOOH enhancements in terms of potential reasons for the model underpredictions, employing as a comparison metric the normalized excess mixing ratios (NEMR) relative to CO. The NEMR is commonly used to quantify dilution-corrected above-background plume enhancements: at-source, the NEMR corresponds to a molar emission ratio (ER), while downwind values also reflect ensuing production and loss. We performed a case-by-case identification of plumes intercepted during ATom meeting any two of the following criteria: (a) peak HCOOH > 1 ppb, (b) peak BC > 100 ng/m^3, and (c) peak CO > 175 ppb (using one-second data in all cases). In this way, 53 plume intercepts were identified during ATom-3 and ATom-4 ranging from <1 min to >20 min duration. Plume identification, NEMR calculation, and source attribution are described for each intercept in the Supporting Information (Table S4, Section S2). In particular, we find that 38 of the 53 identified plume intercepts exhibit clear biomass burning signatures and are thus treated as fire plumes in the analyses that follow. The remaining 15 are likely to be partly or mainly anthropogenic.

https://doi.org/10.1021/acsearthspacechem.1c00049
ACS Earth Space Chem. 2021, 5, 1436−1454

HCOOH enhancements across all 53 plume intercepts vary from ~1 to >30 ppb, with corresponding CO enhancements of 9−270 ppb. The resulting HCOOH NEMRs (calculated for each plume intercept as the reduced major axis HCOOH:CO slope; Table S4 and Figure 6) range from 3.4 ppt/ppb CO in the northern Pacific (plume intercept #19, Section S2) to >200 ppt/ppb CO in plumes with potential mixed urban/anthropogenic influence (plume intercepts #50−53, Section S2).

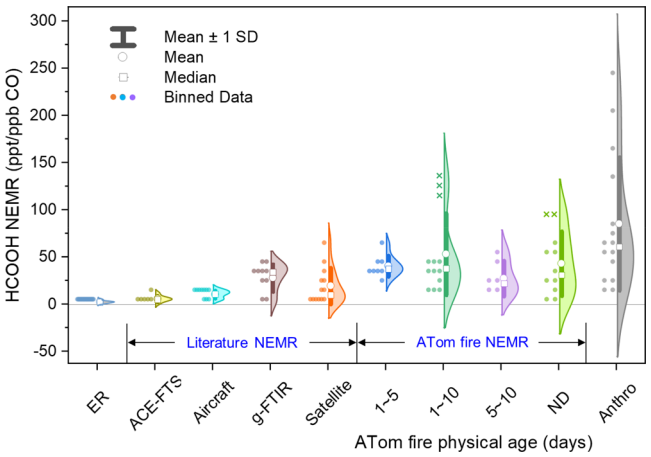

Figure 6. HCOOH normalized excess mixing ratios (NEMRs) relative to CO as a function of transport time for ATom plumes and comparison to prior studies. Transport times (ND: not determined) are estimated based on back-trajectory analysis as described in text. Colored dots indicate fire plumes and plumes with anthropogenic influence (gray). Plumes marked with an "×" denote encounters after a mid-flight instrumental change on 05/14/2018 (see text). Also shown are primary HCOOH emission ratios (ER) as compiled by Andreae[125] and Akagi et al.,[71] and HCOOH NEMR estimates inferred from prior atmospheric observations. These include aircraft studies featuring downwind plume sampling (up to 4.5 h of aging),[27,31,105,121] ground-based remote sensing by Fourier transform infrared spectrometry (g-FTIR),[34,135−137] and space-based observations from the ACE-FTS[29,30,123,124,138,139] and TES/IASI satellite instruments.[32,33,140]

3.4.1. Case Study: Large HCOOH Enhancements in African Plumes. We find that 19 of the 53 identified plume intercepts are due to African fires (with 15 from northwest Africa and 4 from southern Africa; Section S2.1). Of these, plume intercept #40 off the African coast (~16 UTC on 05/14/2018; Figure 7a) featured HCOOH mixing ratios exceeding 15−30 ppb—the highest values seen across all of ATom. Highly enhanced levels of CO (~350 ppb), HCN (~1.5 ppb), and BC (~2 $\mu g/m^3$) were also observed. Back-trajectory analysis indicates that the above plume underwent >2 days of transport after emission in northwest Africa before being intercepted by the aircraft (Figure 7c and Section S2.1). Explaining the observed in-plume HCOOH mixing ratios requires (i) sufficiently large primary HCOOH emissions that 15−30 ppb still remained after >2 days of dilution, (ii) strong secondary HCOOH production during plume aging, or (iii) some combination of the two. HCOOH enhancements this large have only been reported once previously: for a fresh grass fire plume in Southern Africa.[105] In that case, the HCOOH enhancement dropped to 5 ppb after 30 min and to below the detection limit after 40 min. Most other in situ studies (even those conducted near-source) have reported HCOOH mixing ratios below 12 ppb.[5,9,106−111]

The same 05/14/2018 ATom-4 flight included a total of 8 plume intercepts identified as fire outflow from west Africa, and HCOOH:CO NEMR values were quantified for 7 of these (the 8th occurred during an instrument zeroing procedure). Figure 7 shows that HCOOH exhibits quite different behavior from other species sampled across these plumes. HCN and BC, primary fire tracers that are unreactive toward OH, exhibit similar NEMRs across the 7 plume intercepts that are within the range of literature-reported ERs for relevant fire types (savanna, tropical forest, agriculture). Benzene, a primary combustion tracer that is more photochemically reactive (τ = 4.8 days at OH = 2×10^6 molecules/cm^3 and $k_{benzene + OH} = 1.2 \times 10^{-12}$ cm^3/molecule/s[112]), exhibits NEMRs 44−78% lower than the expected primary ERs—consistent with a few days of aging. Acetaldehyde likewise exhibits NEMR values lower than its primary ERs, reflecting the net effect of direct emissions, secondary production, and a short photochemical lifetime. NEMR values for acetone, on the other hand, are 1.4−4.2 times higher than the corresponding ERs and indicate net secondary production during plume aging.[113,114] Methanol, despite having a photochemical lifetime similar to benzene, exhibits NEMR values consistent with its primary ERs, likely reflecting in-plume secondary production offsetting chemical loss[115−117]—as also inferred from the ATom observations by Bates et al.[118] The I-CIMS instrument underwent an operational change at ~14:30 UTC during this flight, which may explain the HCOOH NEMR bifurcation shown in Figure 7. However, even if we take the conservative assumption that the post-14:30 HCOOH NEMRs on this flight should be reduced by ~2 times to match the earlier values, Figure 7 shows that HCOOH is unique among the plotted tracers in exhibiting in-plume NEMRs 1−2 orders of magnitude higher than expected primary ERs—suggesting substantial secondary production en route.

3.4.2. HCOOH NEMR Variability and Relationship with Plume Age. HCOOH NEMRs vary significantly across the ATom plumes investigated here. Values range from a low of 3.4 ppt/ppb CO in a high-altitude fire plume over the North Pacific (plume intercept #19, flight 20171027; the same plume featured the highest HCN mixing ratios encountered during ATom) to >50 ppt/ppb CO. Particularly high NEMR values were observed in a number of plumes that appear to contain a mixture of biomass burning and urban/anthropogenic contributions (Section S2.2 and Figure 6). These large HCOOH enhancements (e.g., >200 ppt/ppb CO for California plumes encountered near the end of ATom-4) may reflect accelerated oxidation of VOC-rich biomass burning emissions in the presence of ample anthropogenic NO_x.[119,120]

The highest HCOOH NEMRs seen during ATom and highlighted above exceed any values reported previously in fire emissions or urban plumes. However, HCOOH has not been routinely measured in airborne fire campaigns, and prior studies including HCOOH measurements have focused on relatively fresh plumes (<4.5 h) without characterizing their longer-term evolution. For example, Goode et al.[121] studied the evolution of two Alaskan forest fire plumes and found that the HCOOH NEMR doubled (from 6−8 to 12−16 ppt/ppb CO) after 2−3 h of evolution. An immediate increase of the HCOOH NEMR (to 10 ppt/ppb CO) was observed in the first 20 min after emission from a savanna fire in southern Africa, but this was soon followed by a decrease to below the

https://doi.org/10.1021/acsearthspacechem.1c00049
ACS Earth Space Chem. 2021, 5, 1436−1454

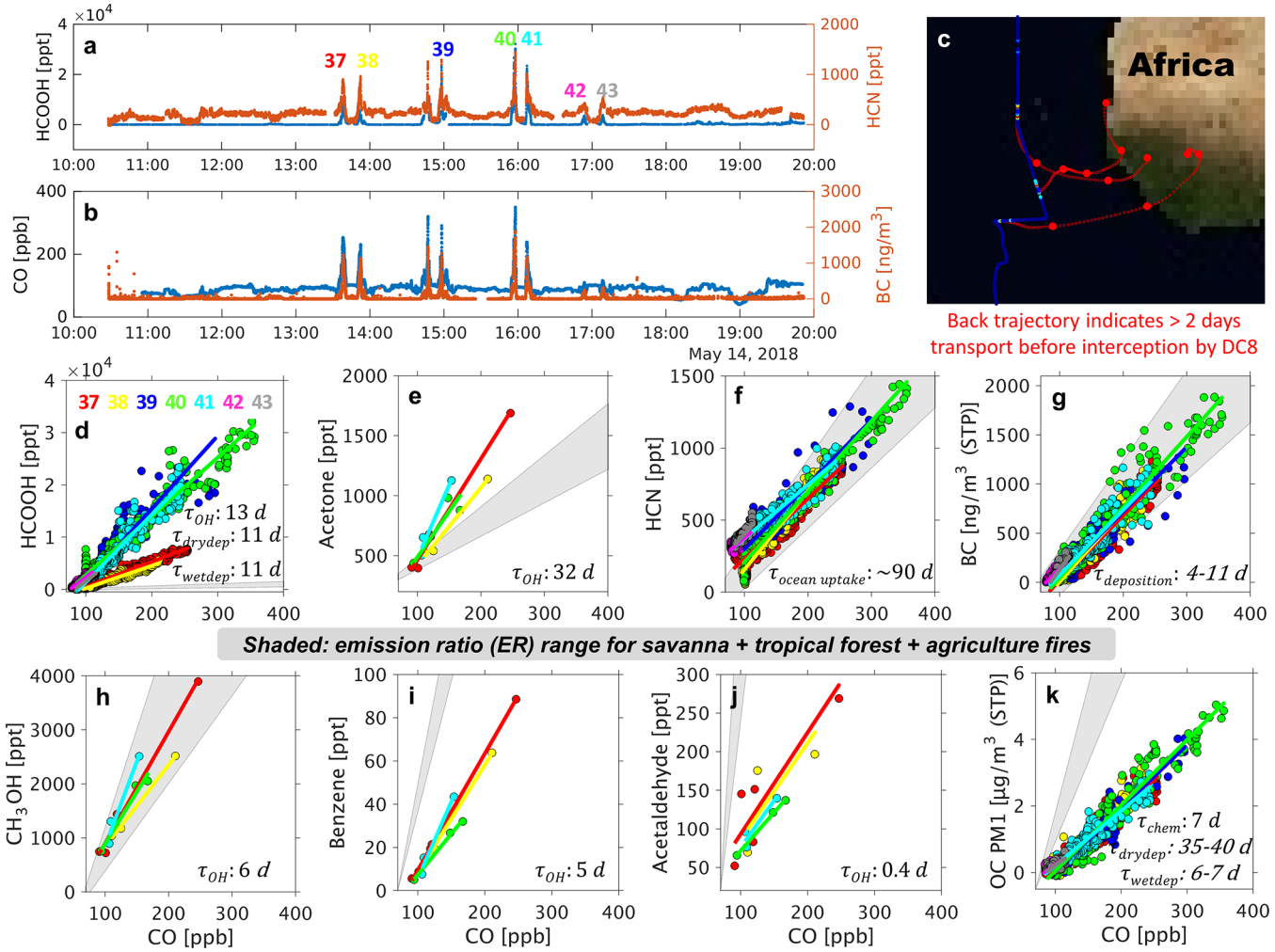

Figure 7. Aged west African fire plumes sampled on 05/14/2018. Panels (a) and (b) show HCOOH, HCN, CO, and BC time series for the entire flight, with 7 plume intercepts (#37−43) marked inset. An additional plume (between #38 and #39) was encountered during a HCOOH instrumental zero and is therefore omitted. Panel (c) shows HYSPLIT back trajectories (red, 1 day intervals marked) for 3 example plume intercepts. Panels (d)−(k) show correlations between select pyrogenic species and CO for all plume intercepts. The resulting NEMR range (obtained from the regression slopes for the 7 plume intercepts) is compared to expected primary emission ratios (ER, shaded in gray) for that species based on compiled data ranges for relevant fuel types (forests, savanna and grassland, and agricultural residue[125]). For TOGA-measured species, only plume intercepts including 3 or more data points (#37, #38, #40, #41) are retained for NEMR analysis. Convective influence is negligible for these plumes based on back-trajectory analysis. The lifetime (unit: days) is shown for each species with respect to its dominant loss pathway.[5,141−144] An OH concentration of 2×10^6 molecules/cm^3 is used to calculate nominal lifetimes to OH oxidation.[145,146]

instrumental detection limit.[105] During MILAGRO, the HCOOH NEMR in a tropical fire plume was observed to increase at a rate of 0.0033/h (from 2.5 to ∼5 ppt/ppb CO) over the first 1.5 h of aging.[31] Akagi et al.[27] reported for a prescribed chaparral fire plume in California that the HCOOH NEMR increased by a factor of 7 (from 0.7 to 4.8 ppt/ppb CO) over 4−4.5 h of aging. Finally, Yokelson et al.[31] reported an even higher NEMR for total organic acids of up to 180 ppt C/ppb CO in aged smoke, but they did not specify the fraction due to HCOOH. In the case of urban/anthropogenic sources,[11] direct HCOOH emissions have been found to be relatively small (∼1 ppt/ppb CO[106,109,110]) with subsequent secondary production yielding enhancements of up to ∼20 ppt/ppb CO.[122]

Enhanced HCOOH levels in fire plumes have also been quantified using remote sensing observations. Tereszchuk et al.[123,124] combined ACE-FTS data with trajectory modeling to examine the evolution of pyrogenic trace species in biomass burning plumes from a variety of geographic regions and found a net decrease of the HCOOH NEMR over 7 days of aging. More recently, satellite data from IASI[33] and TES[32] have been used to study the HCOOH source from key biomass burning regions, with the latter study inferring substantially higher enhancement ratios than expected solely from direct emissions—indicating significant secondary HCOOH production in fire plumes.

One hypothesis to explain the variable HCOOH enhancements observed during ATom is that longer plume transport times and hence aging lead to additional net HCOOH production. We test this idea by estimating physical plume ages for the identified fire intercepts. Ages are computed for each minute of the intercept window as the time since the most recent fire influence based on back-trajectory analysis (Methods; Section S2). We find in this way that the 53 identified plume intercepts can be categorized as follows: (i) one single unambiguous transport time, (ii) a unimodal transport time distribution, (iii) a multimodal transport time distribution, (iv) variable trajectory cluster results across the

https://doi.org/10.1021/acsearthspacechem.1c00049
ACS Earth Space Chem. 2021, 5, 1436−1454

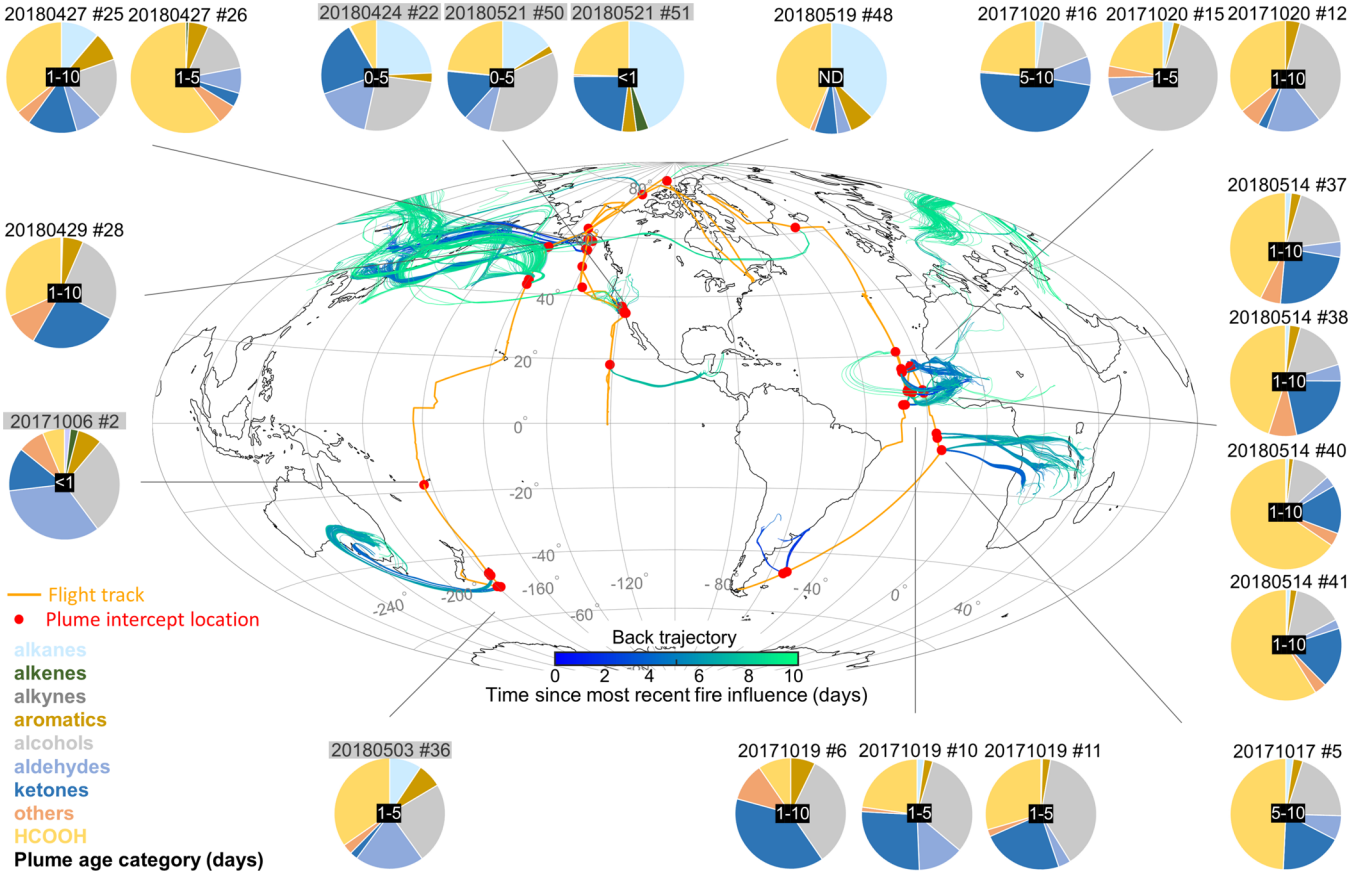

Figure 8. Gas-phase reactive organic carbon (gROC) composition in ATom-3 and ATom-4 fire plumes. Gray shaded intercept numbers reflect plumes with anthropogenic influence. Identified plumes (filled red circles) are denoted along the flight tracks (orange lines) with associated back-trajectory clusters colored by the time since the most recent fire influence. Plumes and trajectories shown are restricted to those with identified fire influence within the previous 10 days. Pie charts show in-plume gROC speciation on an NEMR basis (ppt C/ppb CO). VOCs that are measured only with the WAS system are omitted here for consistency across plumes; Figure S5 includes such species when available. See Figure S6 for a version of this figure that includes submicron aerosol OC.

plume intercept window, and (v) low fire influence probability based on the back trajectories and therefore an undetermined age. We then obtain a best-estimate transport time for each plume intercept from the ensemble of trajectory results across the intercept. Finally, we group the results into plume age categories of (a) <1 day, (b) 1−5 days, (c) 5−10 days, (d) >10 days, or (e) a mixture of two neighboring classes within (a)−(d). More details on this classification process are provided in Section S2.

Figure 6 shows the resulting HCOOH:CO plume-age dependence for the ATom dataset in relation to prior NEMR observations and direct pyrogenic emission ratios. We see that the strongest enhancements (>100 ppt/ppb CO) manifest for aged and anthropogenically influenced plumes (with their likely faster chemistry). Conceptually, we expect increasing NEMRs during early plume aging if the rate of secondary HCOOH production exceeds that of CO, with a subsequent decrease as the plume age approaches the HCOOH photochemical lifetime and precursor VOCs become depleted. The mean trend in Figure 6 does not contradict this expectation, but the main emergent feature is that of highly variable HCOOH enhancements across plumes, with NEMRs spanning a factor of 50 or more within individual age classes. While our trajectory-based plume age estimation and the instrumental calibration for HCOOH (Section 2.1.1) both have some inherent uncertainty, it appears that this remaining variability must mainly reflect other factors such as the source type and burn conditions that affect the HCOOH ER and subsequent plume chemistry.

3.4.3. HCOOH as a Major C Reservoir in Aged Plumes. Figure 8 presents a global view of the gas-phase reactive organic carbon (ROC) composition of the plumes encountered during ATom-3 and ATom-4. We define ROC here to include all VOCs measured during ATom with sufficient in-plume sampling coverage to determine regression-based NEMRs, plus submicron aerosol OC (Section S3). We see in the map that plumes span a wide range of intercept locations, source regions, and transit times, including transported Eurasian fire plumes sampled over the Arctic, Alaska, and the north Pacific; plumes from the northwestern US/southwestern Canada sampled over California; Central American fire plumes sampled over the equatorial Pacific; plumes downwind of Australia, South America, and Africa; and near-source plumes sampled over California and Fiji.

The pie charts in Figure 8 quantify the gas-phase ROC (gROC) composition for selected sampled plumes on an NEMR basis (ppt C/ppb CO). The 21 plume intercepts shown (of 53 total) reflect those with sampling coverage for the I-CIMS, CF_3O^- CIMS, ISAF, and TOGA instruments (see Methods). VOCs measured only by WAS (with its lower temporal resolution) are excluded to prevent species coverage differences between plumes. Figure S5 shows that including

https://doi.org/10.1021/acsearthspacechem.1c00049
ACS Earth Space Chem. 2021, 5, 1436−1454

these species (when available) changes the HCOOH contribution by 1−26% on an NEMR basis.

We see for the plumes plotted in Figure 8 that HCOOH, with NEMRs ranging from 11 to 129 ppt/ppb CO, accounts for between 6 and 60% of the total detected gROC enhancements. This fractional contribution depends on measurement coverage, which is incomplete as ATom was not explicitly a biomass-burning focused mission. Based on prior estimates for the importance of unmeasured/unidentified pyrogenic VOCs,[71] the HCOOH fractions in Figure 8 (and Figure S5) could be 2−3 times lower if all species were accounted for.

The lowest HCOOH contributions (6−23%) are seen for relatively near-source plumes over California and Fiji, contrasting with >30% contributions for several transported Asian and African plumes. Figure S6 shows that, when we expand the analysis to include both gas and particle-phase OC, OC is frequently the largest component of the in-plume ROC enhancement. However, HCOOH still typically contributes between 4 and 33% of the total gas + particle ROC enhancements shown in Figure S6. HCOOH therefore represents a surprisingly large fraction of the detected ROC pool in these plumes, despite being only a small component of primary biomass burning and anthropogenic ROC emissions. As a result, when not subject to wet deposition, HCOOH can be an important pathway for transporting combustion-emitted reactive carbon to the remote atmosphere.

3.4.4. Implied In-Plume HCOOH Production Greater than Predicted from Known Precursors. The fact that the HCOOH enhancements observed during ATom are, in most cases, far larger than can be explained solely based on its direct pyrogenic emissions (Figure 6) points to secondary production as the dominant HCOOH source in these plumes. The total summed direct ER for all identified gas + particle-phase ROC components is estimated to range from ∼300 to 500 ppt C/ppb CO across forest, savanna/grassland/shrubland, and cropland fires, which are the predominant global fire types (Table S6).[71,125,126] This increases to ∼500−1200 ppt C/ppb CO when also including estimated emissions of unidentified/unmeasured ROC components.[71] The median HCOOH enhancement observed across the ATom fire plumes of 36 ppt/ppb CO therefore corresponds to approximately 3−7% of the total expected ROC emission from fires on an NEMR basis.

However, only a fraction of fire-emitted ROC species have been identified as HCOOH precursors, including alkenes (ethene, propene, butene, isoprene, monoterpenes), ethyne, several OVOCs (methyl vinyl ketone, methacrolein, acetaldehyde), hydroxyacetone, hydroxyacetaldehyde, and submicron aerosol OC (Table S6).[17,18,21,23,127−130] The summed direct ER for these known gas-phase HCOOH precursors is estimated to range from 91 to 189 ppt C/ppb CO for forest, savanna/grassland/shrubland, and cropland fires (Table S6). Accounting for the median in-plume ATom HCOOH enhancement of 36 ppt/ppb CO based on these precursor emissions would thus require an average carbon-based yield of 19−40%—much higher than has been reported.[5,16,130,131] Primary ERs for submicron aerosol OC are estimated at 98−226 ppt C/ppb CO (Table S6); in this case, an average per-carbon HCOOH yield of 16−37% from aerosol OC would be needed to explain a HCOOH enhancement of 36 ppt/ppb CO. Malecha and Nizkorodov[23] reported based on chamber measurements that OA mass is photochemically converted to HCOOH at a rate of 1.9/year. Assuming that photodegradation is the major loss pathway for biomass burning OA (at a similar loss rate as derived in chamber experiments for biogenic/anthropogenic secondary aerosol), a rate of 1.9/year corresponds to a carbon-based HCOOH yield of ∼0.3−3% over 1−10 days of aging, which again is far lower (>10−100 times) than required to account for the ATom observations. Together, the above calculations indicate that additional, unknown production pathways are needed to account for the HCOOH enhancements observed in many of the aged fire plumes sampled by ATom.

4. SUMMARY AND IMPLICATIONS

The ATom campaign sampled from pole-to-pole over the remote Pacific and Atlantic Oceans. Outside of continental plumes, HCOOH concentrations were generally less than 100 ppt with no consistent latitudinal gradient that was detectable. Observed background concentrations in the free troposphere are consistent with prior aircraft profiling of the remote atmosphere and with GEOS-Chem model predictions. We conclude that the missing HCOOH precursors identified in earlier work must be mainly terrestrial in nature and short-lived so that their effects do not manifest throughout the remote atmosphere. Similarly, the missing acetaldehyde source in the remote background atmosphere inferred by Wang et al.[40] apparently does not lead to substantial background HCOOH production.

ATom observations provide signatures of HCOOH removal via wet scavenging and ocean uptake. The contrasting behavior between HCOOH and HCN observed in these situations qualitatively matches expectations in the case of wet scavenging, with stronger removal for the more soluble HCOOH. The GEOS-Chem model appears to be underestimating HCOOH removal via wet scavenging, and this is consistent with a small but positive model bias in many parts of the clean mid-to-upper troposphere. In the case of ocean−atmosphere exchange, we find that, while HCN is consistently depleted in the marine boundary layer, this is only sporadically the case for HCOOH—despite its strong air-to-sea partitioning tendency and seawater undersaturation. We attribute this to that ongoing secondary production in continental outflow that often exceeds the rate of HCOOH dry deposition to the ocean; other processes related to the sea surface[38,39] may also be playing a role.

HCOOH enhancements observed during ATom correlate most strongly with BC and are also closely related to the trajectory-derived time since the fire influence. These findings reveal a significant role for fires in driving remote HCOOH variability and highlight the general influence of biomass burning in the remote atmosphere.[57] Normalized excess mixing ratios (NEMRs) for HCOOH in the fire plumes sampled during ATom are frequently 1−2 orders of magnitude higher than expected solely from its primary emissions, implying substantial secondary production in fire plumes (as found in prior near-source and satellite-based studies). We find that HCOOH is a major reactive carbon reservoir in aged fire plumes (up to 33% of the total gas + particle-phase reactive organic carbon, ROC). Such enhancements are larger than can be explained based on its known pyrogenic precursors and current understanding of its formation pathways.

The range of HCOOH NEMR values across the 38 mainly pyrogenic ATom plumes identified here is consistent with findings from prior satellite-based studies, highlighting the

https://doi.org/10.1021/acsearthspacechem.1c00049
ACS Earth Space Chem. 2021, 5, 1436−1454

potential for using satellite data in future investigations of fire plume aging. Unusually high HCOOH NEMRs observed in several mixed anthropogenic + fire plumes sampled during ATom may reflect the vigorous oxidation that can occur when biomass burning VOCs mix with elevated urban-derived NO_x. Further research is needed to better understand the chemistry and associated air-quality impacts during such urban-fire interactions, which can lead to extreme air pollution events for cities in wildfire-prone areas such as the western US.

Fire plumes sampled during ATom range in age up to ∼10 days. While the largest HCOOH enhancements occur in the aged plumes, observed HCOOH NEMRs are highly variable and do not correlate consistently with plume age. What drives this variability? Answering this question requires dedicated in situ plume Lagrangian sampling that is chemically comprehensive and spans a wider age range than typically covered in field studies (<10 h). Such extended sampling is especially important for relatively long-lived species such as HCOOH (lifetime of ∼weeks). Satellite observations,[132,133] while more limited in species coverage, also have potential for sampling across the entire plume evolution spectrum.

■ ASSOCIATED CONTENT

Supporting Information

The Supporting Information is available free of charge at https://pubs.acs.org/doi/10.1021/acsearthspacechem.1c00049.

(Section S1) Tables S1−S3 and Figures S1−S4: (Table S1) Airborne HCOOH measurements in the remote atmosphere; (Table S2) reported surface seawater + lakewater concentrations of HCOOH and formate; (Table S3) global HCOOH sinks; (Figure S1) correlation between HCOOH and other observed species; (Figure S2) back-trajectory-derived influence from fires, convection, and boundary layer on HCOOH; (Figure S3) modeled vs observed key HCOOH precursors; and (Figure S4) example time series showing MBL enhancements of HCOOH. (Section S2) plume attribution: (Table S4) summary of the 53 identified plume intercepts; (Section S2.1) African fire plume intercepts; (Section S2.2) plumes with unusually high HCOOH:CO NEMRs; (Section S2.3) other fire plume intercepts; and (Section S2.4) other fire plume intercepts with anthropogenic influence. (Section S3) ROC related tables and figures: (Figure S5) same as Figure 8, but including those species measured only by WAS; (Figure S6) same as Figure 8, but including submicron aerosol OC; (Table S5) ROC speciation in Figure 8 and Figures S3 and S4; and (Table S6) primary emission ratios (ERs, ppt C/ppb CO) for fire-emitted ROC species (PDF)

■ AUTHOR INFORMATION

Corresponding Author

Dylan B. Millet − *Department of Soil, Water, and Climate, University of Minnesota, St. Paul, Minnesota 55108, United States;* orcid.org/0000-0003-3076-125X; Email: dbm@umn.edu

Authors

Xin Chen − *Department of Soil, Water, and Climate, University of Minnesota, St. Paul, Minnesota 55108, United States;* orcid.org/0000-0002-0952-0008

J. Andrew Neuman − *NOAA Chemical Sciences Laboratory, Boulder, Colorado 80305, United States; Cooperative Institute for Research in Environmental Sciences, University of Colorado Boulder, Boulder, Colorado 80309, United States*

Patrick R. Veres − *NOAA Chemical Sciences Laboratory, Boulder, Colorado 80305, United States*

Eric A. Ray − *NOAA Chemical Sciences Laboratory, Boulder, Colorado 80305, United States; Cooperative Institute for Research in Environmental Sciences, University of Colorado Boulder, Boulder, Colorado 80309, United States*

Róisín Commane − *Department of Earth and Environmental Sciences, Lamont-Doherty Earth Observatory, Columbia University, New York 10964, United States;* orcid.org/0000-0003-1373-1550

Bruce C. Daube − *Department of Earth and Planetary Sciences, Harvard University, Cambridge, Massachusetts 02138, United States*

Kathryn McKain − *Cooperative Institute for Research in Environmental Sciences, University of Colorado Boulder, Boulder, Colorado 80309, United States; NOAA Global Monitoring Laboratory, Boulder, Colorado 80305, United States*

Joshua P. Schwarz − *NOAA Chemical Sciences Laboratory, Boulder, Colorado 80305, United States*

Joseph M. Katich − *NOAA Chemical Sciences Laboratory, Boulder, Colorado 80305, United States; Cooperative Institute for Research in Environmental Sciences, University of Colorado Boulder, Boulder, Colorado 80309, United States*

Karl D. Froyd − *NOAA Chemical Sciences Laboratory, Boulder, Colorado 80305, United States; Cooperative Institute for Research in Environmental Sciences, University of Colorado Boulder, Boulder, Colorado 80309, United States;* orcid.org/0000-0002-0797-6028

Gregory P. Schill − *NOAA Chemical Sciences Laboratory, Boulder, Colorado 80305, United States; Cooperative Institute for Research in Environmental Sciences, University of Colorado Boulder, Boulder, Colorado 80309, United States;* orcid.org/0000-0002-4084-0317

Michelle J. Kim − *Division of Geological and Planetary Sciences, California Institute of Technology, Pasadena, California 91125, United States*

John D. Crounse − *Division of Geological and Planetary Sciences, California Institute of Technology, Pasadena, California 91125, United States;* orcid.org/0000-0001-5443-729X

Hannah M. Allen − *Division of Chemistry and Chemical Engineering, California Institute of Technology, Pasadena, California 91125, United States*

Eric C. Apel − *Atmospheric Chemistry Observations & Modeling Laboratory, National Center for Atmospheric Research, Boulder, Colorado 80307, United States*

Rebecca S. Hornbrook − *Atmospheric Chemistry Observations & Modeling Laboratory, National Center for Atmospheric Research, Boulder, Colorado 80307, United States*

Donald R. Blake − *Department of Chemistry, University of California, Irvine, California 92697, United States*

Benjamin A. Nault − *Cooperative Institute for Research in Environmental Sciences, University of Colorado Boulder,*

Boulder, Colorado 80309, United States; Department of Chemistry, University of Colorado Boulder, Boulder, Colorado 80309, United States; orcid.org/0000-0001-9464-4787

Pedro Campuzano-Jost − *Cooperative Institute for Research in Environmental Sciences, University of Colorado Boulder, Boulder, Colorado 80309, United States; Department of Chemistry, University of Colorado Boulder, Boulder, Colorado 80309, United States;* orcid.org/0000-0003-3930-010X

Jose L. Jimenez − *Cooperative Institute for Research in Environmental Sciences, University of Colorado Boulder, Boulder, Colorado 80309, United States; Department of Chemistry, University of Colorado Boulder, Boulder, Colorado 80309, United States;* orcid.org/0000-0001-6203-1847

Jack E. Dibb − *Earth Systems Research Center/EOS, University of New Hampshire, Durham, New Hampshire 03824, United States*

Complete contact information is available at: https://pubs.acs.org/10.1021/acsearthspacechem.1c00049

Notes

The authors declare no competing financial interest.

■ ACKNOWLEDGMENTS

This research was primarily supported by the National Aeronautics and Space Administration (Grant NNX14AP89G). We thank Armin Wisthaler and Hanwant Singh for their support of this project. Computing resources were provided by the Minnesota Supercomputing Institute (https://www.msi.umn.edu) at the University of Minnesota. We acknowledge the contributions of Steven Wofsy (Harvard QCLS and ATom CO.X), Daniel Murphy (NOAA CSL PALMS), Paul Wennberg (CIT-CIMS), Bernadett Weinzierl (University of Vienna CAPS), Glenn Wolfe and Thomas Hanisco (NASA GSFC ISAF), Thomas Ryerson (NOAA CSL NO_yO_3), and Robert Talbot (NASA GTE MC/IC). We thank Gordon Novak, Jeffery Pierce, and Anna Hodshire for helpful discussions. ATom was funded by the NASA Earth Venture program through Grant NNX15AJ23G. CIRES researchers (J.A.N., E.A.R., J.M.K., K.D.F., and G.P.S.) acknowledge support from NOAA Cooperative Agreement NA17OAR4320101. NCAR researchers (E.C.A. and R.S.H.) acknowledge support from the National Center for Atmospheric Research, which is a major facility sponsored by the National Science Foundation under Cooperative Agreement 1852977. The CU Boulder HR-AMS team (B.A.N., P.C.-J., and J.L.J.) were supported by NASA Grants NNX15AH33A, 80NSSC19K0124, and 80NSSC18K0630.

■ REFERENCES

(1) Keene, W. C.; Galloway, J. N.; Holden, J. D., Jr. Measurement of weak organic acidity in precipitation from remote areas of the world. *J. Geophys. Res.: Oceans* **1983**, *88*, 5122−5130.

(2) Andreae, M. O.; Talbot, R. W.; Andreae, T. W.; Harriss, R. C. Formic and acetic acid over the central Amazon region, Brazil: 1. Dry season. *J. Geophys. Res.: Atmos.* **1988**, *93*, 1616.

(3) Galloway, J. N.; Likens, G. E.; Keene, W. C.; Miller, J. M. The composition of precipitation in remote areas of the world. *J. Geophys. Res.: Oceans* **1982**, *87*, 8771.

(4) Jacob, D. J. Chemistry of OH in remote clouds and its role in the production of formic acid and peroxymonosulfate. *J. Geophys. Res.: Atmos.* **1986**, *91*, 9807.

(5) Millet, D. B.; Baasandorj, M.; Farmer, D. K.; Thornton, J. A.; Baumann, K.; Brophy, P.; Chaliyakunnel, S.; de Gouw, J. A.; Graus, M.; Hu, L.; Koss, A.; Lee, B. H.; Lopez-Hilfiker, F. D.; Neuman, J. A.; Paulot, F.; Peischl, J.; Pollack, I. B.; Ryerson, T. B.; Warneke, C.; Williams, B. J.; Xu, J. A large and ubiquitous source of atmospheric formic acid. *Atmos. Chem. Phys.* **2015**, *15*, 6283−6304.

(6) Paulot, F.; Wunch, D.; Crounse, J. D.; Toon, G. C.; Millet, D. B.; DeCarlo, P. F.; Vigouroux, C.; Deutscher, N. M.; González Abad, G.; Notholt, J.; Warneke, T.; Hannigan, J. W.; Warneke, C.; de Gouw, J. A.; Dunlea, E. J.; De Mazière, M.; Griffith, D. W. T.; Bernath, P.; Jimenez, J. L.; Wennberg, P. O. Importance of secondary sources in the atmospheric budgets of formic and acetic acids. *Atmos. Chem. Phys.* **2011**, *11*, 1989−2013.

(7) Cady-Pereira, K. E.; Chaliyakunnel, S.; Shephard, M. W.; Millet, D. B.; Luo, M.; Wells, K. C. HCOOH measurements from space: TES retrieval algorithm and observed global distribution. *Atmos. Meas. Tech.* **2014**, *7*, 2297−2311.

(8) Stavrakou, T.; Müller, J. F.; Peeters, J.; Razavi, A.; Clarisse, L.; Clerbaux, C.; Coheur, P. F.; Hurtmans, D.; De Mazière, M.; Vigouroux, C.; Deutscher, N. M.; Griffith, D. W. T.; Jones, N.; Paton-Walsh, C. Satellite evidence for a large source of formic acid from boreal and tropical forests. *Nat. Geosci.* **2012**, *5*, 26−30.

(9) Alwe, H. D.; Millet, D. B.; Chen, X.; Raff, J. D.; Payne, Z. C.; Fledderman, K. Oxidation of Volatile Organic Compounds as the Major Source of Formic Acid in a Mixed Forest Canopy. *Geophys. Res. Lett.* **2019**, *46*, 2940−2948.

(10) Schobesberger, S.; Lopez-Hilfiker, F. D.; Taipale, D.; Millet, D. B.; D'Ambro, E. L.; Rantala, P.; Mammarella, I.; Zhou, P.; Wolfe, G. M.; Lee, B. H.; Boy, M.; Thornton, J. A. High upward fluxes of formic acid from a boreal forest canopy. *Geophys. Res. Lett.* **2016**, *43*, 9342−9351.

(11) Veres, P. R.; Roberts, J. M.; Cochran, A. K.; Gilman, J. B.; Kuster, W. C.; Holloway, J. S.; Graus, M.; Flynn, J.; Lefer, B.; Warneke, C.; de Gouw, J. Evidence of rapid production of organic acids in an urban air mass. *Geophys. Res. Lett.* **2011**, *38*, 1944−8007.

(12) Kesselmeier, J.; Bode, K.; Gerlach, C.; Jork, E. M. Exchange of atmospheric formic and acetic acids with trees and crop plants under controlled chamber and purified air conditions. *Atmos. Environ.* **1998**, *32*, 1765−1775.

(13) Mielnik, A.; Link, M.; Mattila, J.; Fulgham, S. R.; Farmer, D. K. Emission of formic and acetic acids from two Colorado soils. *Environ. Sci. Processes Impacts* **2018**, *20*, 1537−1545.

(14) Fulgham, S. R.; Brophy, P.; Link, M.; Ortega, J.; Pollack, I.; Farmer, D. K. Seasonal Flux Measurements over a Colorado Pine Forest Demonstrate a Persistent Source of Organic Acids. *ACS Earth Space Chem.* **2019**, *3*, 2017−2032.

(15) Friedman, B.; Link, M. F.; Fulgham, S. R.; Brophy, P.; Galang, A.; Brune, W. H.; Jathar, S. H.; Farmer, D. K. Primary and Secondary Sources of Gas-Phase Organic Acids from Diesel Exhaust. *Environ. Sci. Technol.* **2017**, *51*, 10872−10880.

(16) Link, M. F.; Nguyen, T. B.; Bates, K.; Müller, J.-F.; Farmer, D. K. Can Isoprene Oxidation Explain High Concentrations of Atmospheric Formic and Acetic Acid over Forests? *ACS Earth Space Chem.* **2020**, *4*, 730−740.

(17) Neeb, P.; Sauer, F.; Horie, O.; Moortgat, G. K. Formation of hydroxymethyl hydroperoxide and formic acid in alkene ozonolysis in the presence of water vapour. *Atmos. Environ.* **1997**, *31*, 1417−1423.

(18) Hatakeyama, S.; Washida, N.; Akimoto, H. Rate constants and mechanisms for the reaction of hydroxyl (OD) radicals with acetylene, propyne, and 2-butyne in air at 297 ± 2 K. *J. Phys. Chem.* **1986**, *90*, 173−178.

(19) Andrews, D. U.; Heazlewood, B. R.; Maccarone, A. T.; Conroy, T.; Payne, R. J.; Jordan, M. J. T.; Kable, S. H. Photo-tautomerization of acetaldehyde to vinyl alcohol: a potential route to tropospheric acids. *Science* **2012**, *337*, 1203−1206.

(20) Shaw, M. F.; Sztáray, B.; Whalley, L. K.; Heard, D. E.; Millet, D. B.; Jordan, M. J. T.; Osborn, D. L.; Kable, S. H. Photo-tautomerization of acetaldehyde as a photochemical source of formic acid in the troposphere. *Nat. Commun.* **2018**, *9*, 2584.
(21) Molina, M. J.; Ivanov, A. V.; Trakhtenberg, S.; Molina, L. T. Atmospheric evolution of organic aerosol. *Geophys. Res. Lett.* **2004**, *31* (22), L22104.
(22) Park, J.; Gomez, A. L.; Walser, M. L.; Lin, A.; Nizkorodov, S. A. Ozonolysis and photolysis of alkene-terminated self-assembled monolayers on quartz nanoparticles: implications for photochemical aging of organic aerosol particles. *Phys. Chem. Chem. Phys.* **2006**, *8*, 2506−2512.
(23) Malecha, K. T.; Nizkorodov, S. A. Photodegradation of Secondary Organic Aerosol Particles as a Source of Small, Oxygenated Volatile Organic Compounds. *Environ. Sci. Technol.* **2016**, *50*, 9990−9997.
(24) Malecha, K. T.; Cai, Z.; Nizkorodov, S. A. Photodegradation of Secondary Organic Aerosol Material Quantified with a Quartz Crystal Microbalance. *Environ. Sci. Technol. Lett.* **2018**, *5*, 366−371.
(25) Pan, X.; Underwood, J. S.; Xing, J. H.; Mang, S. A.; Nizkorodov, S. A. Photodegradation of secondary organic aerosol generated from limonene oxidation by ozone studied with chemical ionization mass spectrometry. *Atmos. Chem. Phys.* **2009**, *9*, 3851−3865.
(26) Walser, M. L.; Park, J.; Gomez, A. L.; Russell, A. R.; Nizkorodov, S. A. Photochemical aging of secondary organic aerosol particles generated from the oxidation of d-limonene. *J. Phys. Chem. A* **2007**, *111*, 1907−1913.
(27) Akagi, S. K.; Craven, J. S.; Taylor, J. W.; McMeeking, G. R.; Yokelson, R. J.; Burling, I. R.; Urbanski, S. P.; Wold, C. E.; Seinfeld, J. H.; Coe, H.; Alvarado, M. J.; Weise, D. R. Evolution of trace gases and particles emitted by a chaparral fire in California. *Atmos. Chem. Phys.* **2012**, *12*, 1397−1421.
(28) Franco, B.; Clarisse, L.; Stavrakou, T.; Müller, J. F.; Taraborrelli, D.; Hadji-Lazaro, J.; Hannigan, J. W.; Hase, F.; Hurtmans, D.; Jones, N.; Lutsch, E.; Mahieu, E.; Ortega, I.; Schneider, M.; Strong, K.; Vigouroux, C.; Clerbaux, C.; Coheur, P. F. Spaceborne Measurements of Formic and Acetic Acids: A Global View of the Regional Sources. *Geophys. Res. Lett.* **2020**, *47*, No. e2019GL086239.
(29) González Abad, G.; Bernath, P. F.; Boone, C. D.; McLeod, S. D.; Manney, G. L.; Toon, G. C. Global distribution of upper tropospheric formic acid from the ACE-FTS. *Atmos. Chem. Phys.* **2009**, *9*, 8039−8047.
(30) Rinsland, C. P.; Boone, C. D.; Bernath, P. F.; Mahieu, E.; Zander, R.; Dufour, G.; Clerbaux, C.; Turquety, S.; Chiou, L.; McConnell, J. C.; Neary, L.; Kaminski, J. W. First space-based observations of formic acid (HCOOH): Atmospheric Chemistry Experiment austral spring 2004 and 2005 Southern Hemisphere tropical-mid-latitude upper tropospheric measurements. *Geophys. Res. Lett.* **2006**, *33*, L23804.
(31) Yokelson, R. J.; Crounse, J. D.; DeCarlo, P. F.; Karl, T.; Urbanski, S.; Atlas, E.; Campos, T.; Shinozuka, Y.; Kapustin, V.; Clarke, A. D.; Weinheimer, A.; Knapp, D. J.; Montzka, D. D.; Holloway, J.; Weibring, P.; Flocke, F.; Zheng, W.; Toohey, D.; Wennberg, P. O.; Wiedinmyer, C.; Mauldin, L.; Fried, A.; Richter, D.; Walega, J.; Jimenez, J. L.; Adachi, K.; Buseck, P. R.; Hall, S. R.; Shetter, R. Emissions from biomass burning in the Yucatan. *Atmos. Chem. Phys.* **2009**, *9*, 5785−5812.
(32) Chaliyakunnel, S.; Millet, D. B.; Wells, K. C.; Cady-Pereira, K. E.; Shephard, M. W. A Large Underestimate of Formic Acid from Tropical Fires: Constraints from Space-Borne Measurements. *Environ. Sci. Technol.* **2016**, *50*, 5631−5640.
(33) Pommier, M.; Clerbaux, C.; Coheur, P.-F. Determination of enhancement ratios of HCOOH relative to CO in biomass burning plumes by the Infrared Atmospheric Sounding Interferometer (IASI). *Atmos. Chem. Phys.* **2017**, *17*, 11089−11105.
(34) Yamanouchi, S.; Strong, K.; Lutsch, E.; Jones, D. B. A. Detection of HCOOH, CH_3OH, CO, HCN, and C_2H_6 in Wildfire Plumes Transported Over Toronto Using Ground-Based FTIR Measurements From 2002−2018. *J. Geophys. Res.: Atmos.* **2020**, *125*, No. e2019JD031924.
(35) Baboukas, E. D.; Kanakidou, M.; Mihalopoulos, N. Carboxylic acids in gas and particulate phase above the Atlantic Ocean. *J. Geophys. Res.: Atmos.* **2000**, *105*, 14459−14471.
(36) Dibb, J. E.; Arsenault, M. Shouldn't snowpacks be sources of monocarboxylic acids? *Atmos. Environ.* **2002**, *36*, 2513−2522.
(37) Dibb, J. E.; Talbot, R. W.; Whitlow, S. I.; Shipham, M. C.; Winterle, J.; McConnell, J.; Bales, R. Biomass burning signatures in the atmosphere and snow at Summit, Greenland: An event on 5 August 1994. *Atmos. Environ.* **1996**, *30*, 553−561.
(38) Jones, B. T.; Muller, J. B. A.; O'Shea, S. J.; Bacak, A.; Le Breton, M.; Bannan, T. J.; Leather, K. E.; Booth, A. M.; Illingworth, S.; Bower, K.; Gallagher, M. W.; Allen, G.; Shallcross, D. E.; Bauguitte, S. J. B.; Pyle, J. A.; Percival, C. J. Airborne measurements of HC(O) OH in the European Arctic: A winter − summer comparison. *Atmos. Environ.* **2014**, *99*, 556−567.
(39) Mungall, E. L.; Abbatt, J. P. D.; Wentzell, J. J. B.; Lee, A. K. Y.; Thomas, J. L.; Blais, M.; Gosselin, M.; Miller, L. A.; Papakyriakou, T.; Willis, M. D.; Liggio, J. Microlayer source of oxygenated volatile organic compounds in the summertime marine Arctic boundary layer. *Proc. Natl. Acad. Sci. U. S. A.* **2017**, *114*, 6203−6208.
(40) Wang, S.; Hornbrook, R. S.; Hills, A.; Emmons, L. K.; Tilmes, S.; Lamarque, J.-F.; Jimenez, J. L.; Campuzano-Jost, P.; Nault, B. A.; Crounse, J. D.; Wennberg, P. O.; Ryerson, T. B.; Thompson, C. R.; Peischl, J.; Moore, F.; Nance, D.; Hall, B.; Elkins, J.; Tanner, D.; Gregory Huey, L.; Hall, S. R.; Ullmann, K.; Orlando, J. J.; Tyndall, G. S.; Flocke, F. M.; Ray, E.; Hanisco, T. F.; Wolfe, G. M.; St Clair, J.; Commane, R.; Daube, B.; Barletta, B.; Blake, D. R.; Weinzierl, B.; Dollner, M.; Conley, A.; Vitt, F.; Wofsy, S. C.; Riemer, D. D. Atmospheric Acetaldehyde: Importance of Air-Sea Exchange and a Missing Source in the Remote Troposphere. *Geophys. Res. Lett.* **2019**, *46*, 5601−5613.
(41) Wofsy, S. C., Afshar, S., Allen, H. M., Apel, E., Asher, E. C., Barletta, B., Bent, J., Bian, H., Biggs, B. C., Blake, D. R., Blake, N., Bourgeois, I., Brock, C. A., Brune, W. H., Budney, J. W., Bui, T. P., Butler, A., Campuzano-Jost, P., Chang, C. S., Chin, M., Commane, R., Correa, G., Crounse, J. D., Cullis, P. D., Daube, B. C., Day, D. A., Dean-Day, J. M., Dibb, J. E., DiGangi, J. P., Diskin, G. S., Dollner, M., Elkins, J. W., Erdesz, F., Fiore, A. M., Flynn, C. M., Froyd, K., Gesler, D. W., Hall, S. R., Hanisco, T. F., Hannun, R. A., Hills, A. J., Hintsa, E. J., Hoffman, A., Hornbrook, R. S., Huey, L. G., Hughes, S., Jimenez, J. L., Johnson, B. J., Katich, J. M., Keeling, R. F., Kim, M. J., Kupc, A., Lait, L. R., Lamarque, J.-F., Liu, J., McKain, K., Mclaughlin, R. J., Meinardi, S., Miller, D. O., Montzka, S. A., Moore, F. L., Morgan, E. J., Murphy, D. M., Murray, L. T., Nault, B. A., Neuman, J. A., Newman, P. A., Nicely, J. M., Pan, X., Paplawsky, W., Peischl, J., Prather, M. J., Price, D. J., Ray, E., Reeves, J. M., Richardson, M., Rollins, A. W., Rosenlof, K. H., Ryerson, T. B., Scheuer, E., Schill, G. P., Schroder, J. C., Schwarz, J. P., St. Clair, J. M., Steenrod, S. D., Stephens, B. B., Strode, S. A., Sweeney, C., Tanner, D., Teng, A. P., Thames, A. B., Thompson, C. R., Ullmann, K., Veres, P. R., Vieznor, N., Wagner, N. L., Watt, A., Weber, R., Weinzierl, B., Wennberg, P., Williamson, C. J., Wilson, J. C., Wolfe, G. M., Woods, C. T., Zeng, L. H., ATom: Merged Atmospheric Chemistry, Trace Gases, and Aerosols. ORNL DAAC, Oak Ridge, Tennessee, USA. 2018, DOI: 10.3334/ornldaac/1581.
(42) Prather, M. J.; Zhu, X.; Flynn, C. M.; Strode, S. A.; Rodriguez, J. M.; Steenrod, S. D.; Liu, J.; Lamarque, J.-F.; Fiore, A. M.; Horowitz, L. W.; Mao, J.; Murray, L. T.; Shindell, D. T.; Wofsy, S. C. Global atmospheric chemistry − which air matters. *Atmos. Chem. Phys.* **2017**, *17*, 9081−9102.
(43) Veres, P. R.; Neuman, J. A.; Bertram, T. H.; Assaf, E.; Wolfe, G. M.; Williamson, C. J.; Weinzierl, B.; Tilmes, S.; Thompson, C. R.; Thames, A. B.; Schroder, J. C.; Saiz-Lopez, A.; Rollins, A. W.; Roberts, J. M.; Price, D.; Peischl, J.; Nault, B. A.; Moller, K. H.; Miller, D. O.; Meinardi, S.; Li, Q.; Lamarque, J. F.; Kupc, A.; Kjaergaard, H. G.; Kinnison, D.; Jimenez, J. L.; Jernigan, C. M.; Hornbrook, R. S.; Hills, A.; Dollner, M.; Day, D. A.; Cuevas, C. A.; Campuzano-Jost, P.;

Burkholder, J.; Bui, T. P.; Brune, W. H.; Brown, S. S.; Brock, C. A.; Bourgeois, I.; Blake, D. R.; Apel, E. C.; Ryerson, T. B. Global airborne sampling reveals a previously unobserved dimethyl sulfide oxidation mechanism in the marine atmosphere. *Proc. Natl. Acad. Sci. U. S. A.* **2020**, *117*, 4505−4510.
(44) Veres, P.; Gilman, J. B.; Roberts, J. M.; Kuster, W. C.; Warneke, C.; Burling, I. R.; de Gouw, J. Development and validation of a portable gas phase standard generation and calibration system for volatile organic compounds. *Atmos. Meas. Tech.* **2010**, *3*, 683−691.
(45) McKain, K., Sweeney, C., Readme for NOAA-Picarro on ATom-1,2,3,4. 2018, https://espo.nasa.gov/sites/default/files/archive_docs/NOAA-Picarro_ATom1234_readme.pdf.
(46) Commane, R.; Budney, J. W.; Gonzalez ramos, Y.; Sargent, M.; Wofsy, S. C.; Daube, B. C. ATom: Measurements from the Quantum Cascade Laser System (QCLS). ORNL DAAC, Oak Ridge, Tennessee, USA, 2020, DOI: 10.3334/ORNLDAAC/1747.
(47) Allen, H. M.; Crounse, J. D.; Kim, M. J.; Teng, A. P.; Wennberg, P. O. ATom: L2 In Situ Data from Caltech Chemical Ionization Mass Spectrometer (CIT-CIMS). ORNL DAAC, Oak Ridge, Tennessee, USA, 2019, DOI: 10.3334/ORNLDAAC/1713.
(48) Crounse, J. D.; McKinney, K. A.; Kwan, A. J.; Wennberg, P. O. Measurement of gas-phase hydroperoxides by chemical ionization mass spectrometry. *Anal. Chem.* **2006**, *78*, 6726−6732.
(49) Hanisco, T. F.; Bian, H.; Nicely, J. M.; Pan, X.; Hannun, R. A.; St.Clair, J. M.; Wolfe, G. M. ATom: L2 Measurements of In Situ Airborne Formaldehyde (ISAF). ORNL DAAC, Oak Ridge, Tennessee, USA, 2019, DOI: 10.3334/ORNLDAAC/1730.
(50) Cazorla, M.; Wolfe, G. M.; Bailey, S. A.; Swanson, A. K.; Arkinson, H. L.; Hanisco, T. F. A new airborne laser-induced fluorescence instrument for in situ detection of formaldehyde throughout the troposphere and lower stratosphere. *Atmos. Meas. Tech.* **2015**, *8*, 541−552.
(51) Apel, E. C.; Asher, E. C.; Hills, A. J.; Hornbrook, R. S. ATom: L2 Volatile Organic Compounds (VOCs) from the Trace Organic Gas Analyzer (TOGA). ORNL DAAC, Oak Ridge, Tennessee, USA, 2019, DOI: 10.3334/ORNLDAAC/1749.
(52) Barletta, B.; Biggs, B. C.; Blake, D. R.; Blake, N.; Hoffman, A.; Hughes, S.; Meinardi, S.; Vieznor, N.; Woods, C. T. ATom: L2 Halocarbons and Hydrocarbons from the UC-Irvine Whole Air Sampler (WAS). ORNL DAAC, Oak Ridge, Tennessee, USA, 2019, DOI: 10.3334/ORNLDAAC/1751.
(53) Ryerson, T. B.; Thompson, C. R.; Peischl, J.; Bourgeois, I. ATom: L2 In Situ Measurements from NOAA Nitrogen Oxides and Ozone (NO_yO_3) Instrument. ORNL DAAC, Oak Ridge, Tennessee, USA, 2019, DOI: 10.3334/ORNLDAAC/1734.
(54) Schwarz, J. P.; Katich, J. M. ATom: L2 In Situ Measurements from Single Particle Soot Photometer (SP2). ORNL DAAC, Oak Ridge, Tennessee, USA, 2019, DOI: 10.3334/ORNLDAAC/1672.
(55) Jimenez, J. L.; Campuzano-Jost, P.; Day, D. A.; Nault, B. A.; Price, D. J.; Schroder, J. C. ATom: L2 Measurements from CU High-Resolution Aerosol Mass Spectrometer (HR-AMS). ORNL DAAC, Oak Ridge, Tennessee, USA, 2019, DOI: 10.3334/ORNLDAAC/1716.
(56) Hodzic, A.; Campuzano-Jost, P.; Bian, H.; Chin, M.; Colarco, P. R.; Day, D. A.; Froyd, K. D.; Heinold, B.; Jo, D. S.; Katich, J. M.; Kodros, J. K.; Nault, B. A.; Pierce, J. R.; Ray, E.; Schacht, J.; Schill, G. P.; Schroder, J. C.; Schwarz, J. P.; Sueper, D. T.; Tegen, I.; Tilmes, S.; Tsigaridis, K.; Yu, P.; Jimenez, J. L. Characterization of organic aerosol across the global remote troposphere: a comparison of ATom measurements and global chemistry models. *Atmos. Chem. Phys.* **2020**, *20*, 4607−4635.
(57) Schill, G. P.; Froyd, K. D.; Bian, H.; Kupc, A.; Williamson, C.; Brock, C. A.; Ray, E.; Hornbrook, R. S.; Hills, A. J.; Apel, E. C.; Chin, M.; Colarco, P. R.; Murphy, D. M. Widespread biomass burning smoke throughout the remote troposphere. *Nat. Geosci.* **2020**, *13*, 422−427.
(58) Spanu, A.; Dollner, M.; Gasteiger, J.; Bui, T. P.; Weinzierl, B. Flow-induced errors in airborne in situ measurements of aerosols and clouds. *Atmos. Meas. Tech.* **2020**, *13*, 1963−1987.
(59) GEOS-Chem 12.1.1, 2018, DOI: 10.5281/zenodo.2249246.
(60) Bian, H.; Prather, M. J. Fast-J2: Accurate Simulation of Stratospheric Photolysis in Global Chemical Models. *J. Atmos. Chem.* **2002**, *41*, 281−296.
(61) Mao, J.; Jacob, D. J.; Evans, M. J.; Olson, J. R.; Ren, X.; Brune, W. H.; Clair, J. M. S.; Crounse, J. D.; Spencer, K. M.; Beaver, M. R.; Wennberg, P. O.; Cubison, M. J.; Jimenez, J. L.; Fried, A.; Weibring, P.; Walega, J. G.; Hall, S. R.; Weinheimer, A. J.; Cohen, R. C.; Chen, G.; Crawford, J. H.; McNaughton, C.; Clarke, A. D.; Jaeglé, L.; Fisher, J. A.; Yantosca, R. M.; Le Sager, P.; Carouge, C. Chemistry of hydrogen oxide radicals (HO_x) in the Arctic troposphere in spring. *Atmos. Chem. Phys.* **2010**, *10*, 5823−5838.
(62) Eastham, S. D.; Weisenstein, D. K.; Barrett, S. R. H. Development and evaluation of the unified tropospheric−stratospheric chemistry extension (UCX) for the global chemistry-transport model GEOS-Chem. *Atmos. Environ.* **2014**, *89*, 52−63.
(63) Lin, S.-J.; Rood, R. B. Multidimensional Flux-Form Semi-Lagrangian Transport Schemes. *Mon. Weather Rev.* **1996**, *124*, 2046−2070.
(64) Wu, S.; Mickley, L. J.; Jacob, D. J.; Logan, J. A.; Yantosca, R. M.; Rind, D. Why are there large differences between models in global budgets of tropospheric ozone? *J. Geophys. Res.* **2007**, *112* (D5), D05302.
(65) Lin, J.-T.; McElroy, M. B. Impacts of boundary layer mixing on pollutant vertical profiles in the lower troposphere: Implications to satellite remote sensing. *Atmos. Environ.* **2010**, *44*, 1726−1739.
(66) Hoesly, R. M.; Smith, S. J.; Feng, L.; Klimont, Z.; Janssens-Maenhout, G.; Pitkanen, T.; Seibert, J. J.; Vu, L.; Andres, R. J.; Bolt, R. M.; Bond, T. C.; Dawidowski, L.; Kholod, N.; Kurokawa, J.; Li, M.; Liu, L.; Lu, Z.; Moura, M. C. P.; O'Rourke, P. R.; Zhang, Q. Historical (1750−2014) anthropogenic emissions of reactive gases and aerosols from the Community Emissions Data System (CEDS). *Geosci. Model Dev.* **2018**, *11*, 369−408.
(67) Marais, E. A.; Wiedinmyer, C. Air Quality Impact of Diffuse and Inefficient Combustion Emissions in Africa (DICE-Africa). *Environ. Sci. Technol.* **2016**, *50*, 10739−10745.
(68) Guenther, A. B.; Jiang, X.; Heald, C. L.; Sakulyanontvittaya, T.; Duhl, T.; Emmons, L. K.; Wang, X. The Model of Emissions of Gases and Aerosols from Nature version 2.1 (MEGAN2.1): an extended and updated framework for modeling biogenic emissions. *Geosci. Model Dev.* **2012**, *5*, 1471−1492.
(69) Hu, L.; Millet, D. B.; Baasandorj, M.; Griffis, T. J.; Turner, P.; Helmig, D.; Curtis, A. J.; Hueber, J. Isoprene emissions and impacts over an ecological transition region in the U.S. Upper Midwest inferred from tall tower measurements. *J. Geophys. Res.: Atmos.* **2015**, *120*, 3553−3571.
(70) van der Werf, G. R.; Randerson, J. T.; Giglio, L.; van Leeuwen, T. T.; Chen, Y.; Rogers, B. M.; Mu, M.; van Marle, M. J. E.; Morton, D. C.; Collatz, G. J.; Yokelson, R. J.; Kasibhatla, P. S. Global fire emissions estimates during 1997−2016. *Earth Syst. Sci. Data* **2017**, *9*, 697−720.
(71) Akagi, S. K.; Yokelson, R. J.; Wiedinmyer, C.; Alvarado, M. J.; Reid, J. S.; Karl, T.; Crounse, J. D.; Wennberg, P. O. Emission factors for open and domestic biomass burning for use in atmospheric models. *Atmos. Chem. Phys.* **2011**, *11*, 4039−4072.
(72) Wesely, M. L. Parameterization of surface resistances to gaseous dry deposition in regional-scale numerical models. *Atmos. Environ.* **1989**, *23*, 1293−1304.
(73) Wang, Y.; Jacob, D. J.; Logan, J. A. Global simulation of tropospheric O_3-NO_x-hydrocarbon chemistry: 1. Model formulation. *J. Geophys. Res.: Atmos.* **1998**, *103*, 10713−10725.
(74) Amos, H. M.; Jacob, D. J.; Holmes, C. D.; Fisher, J. A.; Wang, Q.; Yantosca, R. M.; Corbitt, E. S.; Galarneau, E.; Rutter, A. P.; Gustin, M. S.; Steffen, A.; Schauer, J. J.; Graydon, J. A.; Louis, V. L. S.; Talbot, R. W.; Edgerton, E. S.; Zhang, Y.; Sunderland, E. M. Gas-particle partitioning of atmospheric Hg (II) and its effect on global mercury deposition. *Atmos. Chem. Phys.* **2012**, *12*, 591−603.

(75) Mari, C.; Jacob, D. J.; Bechtold, P. Transport and scavenging of soluble gases in a deep convective cloud. *J. Geophys. Res.: Atmos.* **2000**, *105*, 22255−22267.
(76) Bowman, K. P. Large-scale isentropic mixing properties of the Antarctic polar vortex from analyzed winds. *J. Geophys. Res.: Atmos.* **1993**, *98*, 23013.
(77) Bowman, K. P.; Carrie, G. D. The Mean-Meridional Transport Circulation of the Troposphere in an Idealized GCM. *J. Atmos. Sci.* **2002**, *59*, 1502−1514.
(78) Freeborn, P. H.; Wooster, M. J.; Roy, D. P.; Cochrane, M. A. Quantification of MODIS fire radiative power (FRP) measurement uncertainty for use in satellite-based active fire characterization and biomass burning estimation. *Geophys. Res. Lett.* **2014**, *41*, 1988−1994.
(79) Schroeder, W.; Oliva, P.; Giglio, L.; Csiszar, I. A. The New VIIRS 375m active fire detection data product: Algorithm description and initial assessment. *Remote Sens. Environ.* **2014**, *143*, 85−96.
(80) Singh, H. B.; Thompson, A. M.; Schlager, H. SONEX airborne mission and coordinated POLINAT-2 activity: Overview and accomplishments. *Geophys. Res. Lett.* **1999**, *26*, 3053−3056.
(81) Hoell, J. M.; Davis, D. D.; Jacob, D. J.; Rodgers, M. O.; Newell, R. E.; Fuelberg, H. E.; McNeal, R. J.; Raper, J. L.; Bendura, R. J. Pacific Exploratory Mission in the tropical Pacific: PEM-Tropics A, August-September 1996. *J. Geophys. Res.: Atmos.* **1999**, *104*, 5567−5583.
(82) Hoell, J. M.; Davis, D. D.; Liu, S. C.; Newell, R.; Shipham, M.; Akimoto, H.; McNeal, R. J.; Bendura, R. J.; Drewry, J. W. Pacific Exploratory Mission-West A (PEM-West A): September-October 1991. *J. Geophys. Res.: Atmos.* **1996**, *101*, 1641−1653.
(83) Hoell, J. M.; Davis, D. D.; Liu, S. C.; Newell, R. E.; Akimoto, H.; McNeal, R. J.; Bendura, R. J. The Pacific Exploratory Mission-West Phase B: February-March, 1994. *J. Geophys. Res.: Atmos.* **1997**, *102*, 28223−28239.
(84) Kleb, M. M.; Chen, G.; Crawford, J. H.; Flocke, F. M.; Brown, C. C. An overview of measurement comparisons from the INTEX-B/MILAGRO airborne field campaign. *Atmos. Meas. Tech.* **2011**, *4*, 9−27.
(85) Singh, H. B.; Brune, W. H.; Crawford, J. H.; Flocke, F.; Jacob, D. J. Chemistry and transport of pollution over the Gulf of Mexico and the Pacific: spring 2006 INTEX-B campaign overview and first results. *Atmos. Chem. Phys.* **2009**, *9*, 2301−2318.
(86) Fishman, J.; Hoell, J. M.; Bendura, R. D.; McNeal, R. J.; Kirchhoff, V. W. J. H. NASA GTE TRACE A experiment (September-October 1992): Overview. *J. Geophys. Res.: Atmos.* **1996**, *101*, 23865−23879.
(87) Coggon, M. M.; Veres, P. R.; Yuan, B.; Koss, A.; Warneke, C.; Gilman, J. B.; Lerner, B. M.; Peischl, J.; Aikin, K. C.; Stockwell, C. E.; Hatch, L. E.; Ryerson, T. B.; Roberts, J. M.; Yokelson, R. J.; de Gouw, J. A. Emissions of nitrogen-containing organic compounds from the burning of herbaceous and arboraceous biomass: Fuel composition dependence and the variability of commonly used nitrile tracers. *Geophys. Res. Lett.* **2016**, *43*, 9903−9912.
(88) Travis, K. R.; Heald, C. L.; Allen, H. M.; Apel, E. C.; Arnold, S. R.; Blake, D. R.; Brune, W. H.; Chen, X.; Commane, R.; Crounse, J. D.; Daube, B. C.; Diskin, G. S.; Elkins, J. W.; Evans, M. J.; Hall, S. R.; Hintsa, E. J.; Hornbrook, R. S.; Kasibhatla, P. S.; Kim, M. J.; Luo, G.; McKain, K.; Millet, D. B.; Moore, F. L.; Peischl, J.; Ryerson, T. B.; Sherwen, T.; Thames, A. B.; Ullmann, K.; Wang, X.; Wennberg, P. O.; Wolfe, G. M.; Yu, F. Constraining remote oxidation capacity with ATom observations. *Atmos. Chem. Phys.* **2020**, *20*, 7753−7781.
(89) Clubb, A. E.; Jordan, M. J.; Kable, S. H.; Osborn, D. L. Phototautomerization of Acetaldehyde to Vinyl Alcohol: A Primary Process in UV-Irradiated Acetaldehyde from 295 to 335 nm. *J. Phys. Chem. Lett.* **2012**, *3*, 3522−3526.
(90) So, S.; Wille, U.; da Silva, G. Atmospheric chemistry of enols: a theoretical study of the vinyl alcohol + OH + O_2 reaction mechanism. *Environ. Sci. Technol.* **2014**, *48*, 6694−6701.
(91) da Silva, G. Carboxylic acid catalyzed keto-enol tautomerizations in the gas phase. *Angew. Chem., Int. Ed. Engl.* **2010**, *49*, 7523−7525.
(92) Archibald, A. T.; McGillen, M. R.; Taatjes, C. A.; Percival, C. J.; Shallcross, D. E. Atmospheric transformation of enols: A potential secondary source of carboxylic acids in the urban troposphere. *Geophys. Res. Lett.* **2007**, *34* (21), L21801.
(93) Sander, R. Compilation of Henry's law constants (version 4.0) for water as solvent. *Atmos. Chem. Phys.* **2015**, *15*, 4399−4981.
(94) Sander, S. P., Abbatt, J., Barker, J. R., Burkholder, J. B., Friedl, R. R., Golden, D. M., Huie, R. E., Kolb, C. E., Kurylo, M. J., Moortgat, G. K., Orkin, V. L., Wine, P. H., *Chemical Kinetics and Photochemical Data for Use in Atmospheric Studies*, Evaluation No. 17, JPL Publication 10−6, Jet Propulsion Laboratory, Pasadena, available at: https://jpldataeval.jpl.nasa.gov/pdf/JPL%2010-6%20Final%2015June2011.pdf (last access: 29 May 2018), 2011. 2011.
(95) Johnson, B. J.; Betterton, E. A.; Craig, D. Henry's law coefficients of formic and acetic acids. *J. Atmos. Chem.* **1996**, *24*, 113−119.
(96) Singh, H. B.; Salas, L.; Herlth, D.; Kolyer, R.; Czech, E.; Viezee, W.; Li, Q.; Jacob, D. J.; Blake, D.; Sachse, G.; Harward, C. N.; Fuelberg, H.; Kiley, C. M.; Zhao, Y.; Kondo, Y. In situ measurements of HCN and CH_3CN over the Pacific Ocean: Sources, sinks, and budgets. *J. Geophys. Res.* **2003**, *108* (D20), 8795.
(97) Crutzen, P. J.; Lawrence, M. G. The Impact of Precipitation Scavenging on the Transport of Trace Gases: A 3-Dimensional Model Sensitivity Study. *J. Atmos. Chem.* **2000**, *37*, 81−112.
(98) Yu, P.; Froyd, K. D.; Portmann, R. W.; Toon, O. B.; Freitas, S. R.; Bardeen, C. G.; Brock, C.; Fan, T.; Gao, R. S.; Katich, J. M.; Kupc, A.; Liu, S.; Maloney, C.; Murphy, D. M.; Rosenlof, K. H.; Schill, G.; Schwarz, J. P.; Williamson, C. Efficient In-Cloud Removal of Aerosols by Deep Convection. *Geophys. Res. Lett.* **2019**, *46*, 1061−1069.
(99) Koyama, T.; Thoivipson, T. G. Identification and Determination of Organic Acids in Sea Water by Partition Chromatography. *J. Oceanogr. Soc. Jpn.* **1964**, *20*, 209−220.
(100) Hama, T.; Handa, N. Volatile Organic Acids in Lake Water; Their Gas Chromatographic Determination and Ecological Significance. *Japanese Journal of Limnology (Rikusuigaku Zasshi)* **1981**, *42*, 8−19.
(101) Kieber, D. J.; Vaughan, G. M.; Mopper, K. Determination of formate in natural waters by a coupled enzymatic/high-performance liquid chromatographic technique. *Anal. Chem.* **2002**, *60*, 1654−1659.
(102) Vaughan, G. M.; Mopper, K. Determination of nanomolar levels of formate in natural waters based on a luminescence enzymatic assay. *Anal. Chim. Acta* **1990**, *231*, 299−303.
(103) Mopper, K.; Kieber, D. J. Distribution and biological turnover of dissolved organic compounds in the water column of the Black Sea. *Deep Sea Res. Part A* **1991**, *38*, S1021−S1047.
(104) Talaie, A.; Boger, Z.; Romagnoli, J. A.; Adeloju, S. B.; Yuan, Y. J. Data acquisition, signal processing and modelling: a study of a conducting polypyrrole formate biosensor Part 1: Batch experiment. *Synth. Met.* **1996**, *83*, 21−26.
(105) Hobbs, P. V.; Sinha, P.; Yokelson, R. J.; Christian, T. J.; Blake, D. R.; Gao, S.; Kirchstetter, T. W.; Novakov, T.; Pilewskie, P. Evolution of gases and particles from a savanna fire in South Africa. *J. Geophys. Res.: Atmos.* **2003**, *108*, 8485.
(106) Yuan, B.; Veres, P. R.; Warneke, C.; Roberts, J. M.; Gilman, J. B.; Koss, A.; Edwards, P. M.; Graus, M.; Kuster, W. C.; Li, S. M.; Wild, R. J.; Brown, S. S.; Dubé, W. P.; Lerner, B. M.; Williams, E. J.; Johnson, J. E.; Quinn, P. K.; Bates, T. S.; Lefer, B.; Hayes, P. L.; Jimenez, J. L.; Weber, R. J.; Zamora, R.; Ervens, B.; Millet, D. B.; Rappenglück, B.; de Gouw, J. A. Investigation of secondary formation of formic acid: urban environment vs. oil and gas producing region. *Atmos. Chem. Phys.* **2015**, *15*, 1975−1993.
(107) Nah, T.; Ji, Y.; Tanner, D. J.; Guo, H.; Sullivan, A. P.; Ng, N. L.; Weber, R. J.; Huey, L. G. Real-time measurements of gas-phase organic acids using SF_6^- chemical ionization mass spectrometry. *Atmos. Meas. Tech.* **2018**, *11*, 5087−5104.
(108) Mungall, E. L.; Abbatt, J. P. D.; Wentzell, J. J. B.; Wentworth, G. R.; Murphy, J. G.; Kunkel, D.; Gute, E.; Tarasick, D. W.; Sharma, S.; Cox, C. J.; Uttal, T.; Liggio, J. High gas-phase mixing ratios of

formic and acetic acid in the High Arctic. *Atmos. Chem. Phys.* **2018**, *18*, 10237−10254.
(109) Bannan, T. J.; Murray Booth, A.; Le Breton, M.; Bacak, A.; Muller, J. B. A.; Leather, K. E.; Khan, M. A. H.; Lee, J. D.; Dunmore, R. E.; Hopkins, J. R.; Fleming, Z. L.; Sheps, L.; Taatjes, C. A.; Shallcross, D. E.; Percival, C. J. Seasonality of Formic Acid (HCOOH) in London during the Clearf Lo Campaign. *J. Geophys. Res.: Atmos.* **2017**, *122*, 12488−12498.
(110) Li, K.; Li, J.; Tong, S.; Wang, W.; Huang, R.-J.; Ge, M. Characteristics of wintertime VOCs in suburban and urban Beijing: concentrations, emission ratios, and festival effects. *Atmos. Chem. Phys.* **2019**, *19*, 8021−8036.
(111) Brophy, P.; Farmer, D. K. A switchable reagent ion high resolution time-of-flight chemical ionization mass spectrometer for real-time measurement of gas phase oxidized species: characterization from the 2013 southern oxidant and aerosol study. *Atmos. Meas. Tech.* **2015**, *8*, 2945−2959.
(112) IUPAC, http://iupac.pole-ether.fr . 2008.
(113) Jost, C.; Trentmann, J.; Sprung, D.; Andreae, M. O.; McQuaid, J. B.; Barjat, H. Trace gas chemistry in a young biomass burning plume over Namibia: Observations and model simulations. *J. Geophys. Res.: Atmos.* **2003**, *108*, 8482.
(114) Hornbrook, R. S.; Blake, D. R.; Diskin, G. S.; Fried, A.; Fuelberg, H. E.; Meinardi, S.; Mikoviny, T.; Richter, D.; Sachse, G. W.; Vay, S. A.; Walega, J.; Weibring, P.; Weinheimer, A. J.; Wiedinmyer, C.; Wisthaler, A.; Hills, A.; Riemer, D. D.; Apel, E. C. Observations of nonmethane organic compounds during ARCTAS − Part 1: Biomass burning emissions and plume enhancements. *Atmos. Chem. Phys.* **2011**, *11*, 11103−11130.
(115) de Gouw, J. A.; Warneke, C.; Stohl, A.; Wollny, A. G.; Brock, C. A.; Cooper, O. R.; Holloway, J. S.; Trainer, M.; Fehsenfeld, F. C.; Atlas, E. L.; Donnelly, S. G.; Stroud, V.; Lueb, A. Volatile organic compounds composition of merged and aged forest fire plumes from Alaska and western Canada. *J. Geophys. Res.: Atmos.* **2006**, *111*, D10303.
(116) Holzinger, R.; Williams, J.; Salisbury, G.; Klüpfel, T.; de Reus, M.; Traub, M.; Crutzen, P. J.; Lelieveld, J. Oxygenated compounds in aged biomass burning plumes over the Eastern Mediterranean: evidence for strong secondary production of methanol and acetone. *Atmos. Chem. Phys.* **2005**, *5*, 39−46.
(117) Yokelson, R. J.; Bertschi, I. T.; Christian, T. J.; Hobbs, P. V.; Ward, D. E.; Hao, W. M. Trace gas measurements in nascent, aged, and cloud-processed smoke from African savanna fires by airborne Fourier transform infrared spectroscopy (AFTIR). *J. Geophys. Res.: Atmos.* **2003**, *108* (D13), 8478.
(118) Bates, K. H.; Jacob, D. J.; Wang, S.; Hornbrook, R. S.; Apel, E. C.; Kim, M. J.; Millet, D. B.; Wells, K. C.; Chen, X.; Brewer, J. F.; Ray, E.; Commane, R.; Diskin, G. S.; Wofsy, S. C. The global budget of atmospheric methanol: new constraints on secondary, oceanic, and terrestrial sources. *J. Geophys. Res.: Atmos.* **2021**, *126* (4), No. e2020JD033439.
(119) Hecobian, A.; Liu, Z.; Hennigan, C. J.; Huey, L. G.; Jimenez, J. L.; Cubison, M. J.; Vay, S.; Diskin, G. S.; Sachse, G. W.; Wisthaler, A.; Mikoviny, T.; Weinheimer, A. J.; Liao, J.; Knapp, D. J.; Wennberg, P. O.; Kürten, A.; Crounse, J. D.; Clair, J. S.; Wang, Y.; Weber, R. J. Comparison of chemical characteristics of 495 biomass burning plumes intercepted by the NASA DC-8 aircraft during the ARCTAS/CARB-2008 field campaign. *Atmos. Chem. Phys.* **2011**, *11*, 13325−13337.
(120) Singh, H. B.; Cai, C.; Kaduwela, A.; Weinheimer, A.; Wisthaler, A. Interactions of fire emissions and urban pollution over California: Ozone formation and air quality simulations. *Atmos. Environ.* **2012**, *56*, 45−51.
(121) Goode, J. G.; Yokelson, R. J.; Ward, D. E.; Susott, R. A.; Babbitt, R. E.; Davies, M. A.; Hao, W. M. Measurements of excess O_3, CO_2, CO, CH_4, C_2H_4, C_2H_2, HCN, NO, NH_3, HCOOH, CH_3COOH, HCHO, and CH_3OH in 1997 Alaskan biomass burning plumes by airborne Fourier transform infrared spectroscopy (AFTIR). *J. Geophys. Res.: Atmos.* **2000**, *105*, 22147−22166.
(122) de Gouw, J. A.; Gilman, J. B.; Kim, S. W.; Alvarez, S. L.; Dusanter, S.; Graus, M.; Griffith, S. M.; Isaacman-Van Wertz, G.; Kuster, W. C.; Lefer, B. L.; Lerner, B. M.; McDonald, B. C.; Rappenglück, B.; Roberts, J. M.; Stevens, P. S.; Stutz, J.; Thalman, R.; Veres, P. R.; Volkamer, R.; Warneke, C.; Washenfelder, R. A.; Young, C. J. Chemistry of Volatile Organic Compounds in the Los Angeles Basin: Formation of Oxygenated Compounds and Determination of Emission Ratios. *J. Geophys. Res.: Atmos.* **2018**, *123*, 2298−2319.
(123) Tereszchuk, K. A.; González Abad, G.; Clerbaux, C.; Hadji-Lazaro, J.; Hurtmans, D.; Coheur, P. F.; Bernath, P. F. ACE-FTS observations of pyrogenic trace species in boreal biomass burning plumes during BORTAS. *Atmos. Chem. Phys.* **2013**, *13*, 4529−4541.
(124) Tereszchuk, K. A.; González Abad, G.; Clerbaux, C.; Hurtmans, D.; Coheur, P. F.; Bernath, P. F. ACE-FTS measurements of trace species in the characterization of biomass burning plumes. *Atmos. Chem. Phys.* **2011**, *11*, 12169−12179.
(125) Andreae, M. O. Emission of trace gases and aerosols from biomass burning − an updated assessment. *Atmos. Chem. Phys.* **2019**, *19*, 8523−8546.
(126) Giglio, L.; Randerson, J. T.; van der Werf, G. R. Analysis of daily, monthly, and annual burned area using the fourth-generation global fire emissions database (GFED4). *J. Geophys. Res. Biogeosci* **2013**, *118*, 317−328.
(127) Butkovskaya, N. I.; Pouvesle, N.; Kukui, A.; Bras, G. L. Mechanism of the OH-initiated oxidation of glycolaldehyde over the temperature range 233-296 K. *J. Phys. Chem. A* **2006**, *110*, 13492−13499.
(128) Butkovskaya, N. I.; Pouvesle, N.; Kukui, A.; Mu, Y.; Le Bras, G. Mechanism of the OH-initiated oxidation of hydroxyacetone over the temperature range 236-298 K. *J. Phys. Chem. A* **2006**, *110*, 6833−6843.
(129) Leather, K. E.; McGillen, M. R.; Cooke, M. C.; Utembe, S. R.; Archibald, A. T.; Jenkin, M. E.; Derwent, R. G.; Shallcross, D. E.; Percival, C. J. Acid-yield measurements of the gas-phase ozonolysis of ethene as a function of humidity using Chemical Ionisation Mass Spectrometry (CIMS). *Atmos. Chem. Phys.* **2012**, *12*, 469−479.
(130) Lee, A.; Goldstein, A. H.; Kroll, J. H.; Ng, N. L.; Varutbangkul, V.; Flagan, R. C.; Seinfeld, J. H. Gas-phase products and secondary aerosol yields from the photooxidation of 16 different terpenes. *J. Geophys. Res.* **2006**, *111* (D17), D17305.
(131) Friedman, B.; Farmer, D. K. SOA and gas phase organic acid yields from the sequential photooxidation of seven monoterpenes. *Atmos. Environ.* **2018**, *187*, 335−345.
(132) Theys, N.; Volkamer, R.; Müller, J. F.; Zarzana, K. J.; Kille, N.; Clarisse, L.; De Smedt, I.; Lerot, C.; Finkenzeller, H.; Hendrick, F.; Koenig, T. K.; Lee, C. F.; Knote, C.; Yu, H.; Van Roozendael, M. Global nitrous acid emissions and levels of regional oxidants enhanced by wildfires. *Nat. Geosci.* **2020**, *13*, 681−686.
(133) Alvarado, L. M. A.; Richter, A.; Vrekoussis, M.; Hilboll, A.; Kalisz Hedegaard, A. B.; Schneising, O.; Burrows, J. P. Unexpected long-range transport of glyoxal and formaldehyde observed from the Copernicus Sentinel-5 Precursor satellite during the 2018 Canadian wildfires. *Atmos. Chem. Phys.* **2020**, *20*, 2057−2072.
(134) Singh, H.; Chen, Y.; Tabazadeh, A.; Fukui, Y.; Bey, I.; Yantosca, R.; Jacob, D.; Arnold, F.; Wohlfrom, K.; Atlas, E.; Flocke, F.; Blake, D.; Blake, N.; Heikes, B.; Snow, J.; Talbot, R.; Gregory, G.; Sachse, G.; Vay, S.; Kondo, Y. Distribution and fate of selected oxygenated organic species in the troposphere and lower stratosphere over the Atlantic. *J. Geophys. Res.: Atmos.* **2000**, *105*, 3795−3805.
(135) Viatte, C.; Strong, K.; Hannigan, J.; Nussbaumer, E.; Emmons, L. K.; Conway, S.; Paton-Walsh, C.; Hartley, J.; Benmergui, J.; Lin, J. Identifying fire plumes in the Arctic with tropospheric FTIR measurements and transport models. *Atmos. Chem. Phys.* **2015**, *15*, 2227−2246.
(136) Vigouroux, C.; Stavrakou, T.; Whaley, C.; Dils, B.; Duflot, V.; Hermans, C.; Kumps, N.; Metzger, J. M.; Scolas, F.; Vanhaelewyn, G.; Müller, J. F.; Jones, D. B. A.; Li, Q.; De Mazière, M. FTIR time-series of biomass burning products (HCN, C_2H_6, C_2H_2, CH_3OH, and

HCOOH) at Reunion Island (21° S, 55° E) and comparisons with model data. *Atmos. Chem. Phys.* **2012**, *12*, 10367−10385.
(137) Paton-Walsh, C.; Jones, N. B.; Wilson, S. R.; Haverd, V.; Meier, A.; Griffith, D. W. T.; Rinsland, C. P. Measurements of trace gas emissions from Australian forest fires and correlations with coincident measurements of aerosol optical depth. *J. Geophys. Res.* **2005**, *110* (D24), D24305.
(138) Rinsland, C. P.; Dufour, G.; Boone, C. D.; Bernath, P. F.; Chiou, L.; Coheur, P.; Turquety, S.; Clerbaux, C. Satellite boreal measurements over Alaska and Canada during June-July 2004: Simultaneous measurements of upper tropospheric CO, C_2H_6, HCN, CH_3Cl, CH_4, C_2H_2, CH_3OH, HCOOH, OCS, and SF_6 mixing ratios. *Global Biogeochem. Cycles* **2007**, *21* (3), GB3008.
(139) Coheur, P. F.; Herbin, H.; Clerbaux, C.; Hurtmans, D.; Wespes, C.; Carleer, M.; Turquety, S.; Rinsland, C. P.; Remedios, J.; Hauglustaine, D.; Boone, C. D.; Bernath, P. F. ACE-FTS observation of a young biomass burning plume: first reported measurements of C_2H_4, C_3H_6O, H_2CO and PAN by infrared occultation from space. *Atmos. Chem. Phys.* **2007**, *7*, 5437−5446.
(140) R'Honi, Y.; Clarisse, L.; Clerbaux, C.; Hurtmans, D.; Duflot, V.; Turquety, S.; Ngadi, Y.; Coheur, P. F. Exceptional emissions of NH_3 and HCOOH in the 2010 Russian wildfires. *Atmos. Chem. Phys.* **2013**, *13*, 4171−4181.
(141) Li, Q.; Jacob, D. J.; Bey, I.; Yantosca, R. M.; Zhao, Y.; Kondo, Y.; Notholt, J. Atmospheric hydrogen cyanide (HCN): Biomass burning source, ocean sink? *Geophys. Res. Lett.* **2000**, *27*, 357−360.
(142) Hodzic, A.; Kasibhatla, P. S.; Jo, D. S.; Cappa, C. D.; Jimenez, J. L.; Madronich, S.; Park, R. J. Rethinking the global secondary organic aerosol (SOA) budget: stronger production, faster removal, shorter lifetime. *Atmos. Chem. Phys.* **2016**, *16*, 7917−7941.
(143) Tsigaridis, K.; Daskalakis, N.; Kanakidou, M.; Adams, P. J.; Artaxo, P.; Bahadur, R.; Balkanski, Y.; Bauer, S. E.; Bellouin, N.; Benedetti, A.; Bergman, T.; Berntsen, T. K.; Beukes, J. P.; Bian, H.; Carslaw, K. S.; Chin, M.; Curci, G.; Diehl, T.; Easter, R. C.; Ghan, S. J.; Gong, S. L.; Hodzic, A.; Hoyle, C. R.; Iversen, T.; Jathar, S.; Jimenez, J. L.; Kaiser, J. W.; Kirkevåg, A.; Koch, D.; Kokkola, H.; Lee, Y. H.; Lin, G.; Liu, X.; Luo, G.; Ma, X.; Mann, G. W.; Mihalopoulos, N.; Morcrette, J. J.; Müller, J. F.; Myhre, G.; Myriokefalitakis, S.; Ng, N. L.; O'Donnell, D.; Penner, J. E.; Pozzoli, L.; Pringle, K. J.; Russell, L. M.; Schulz, M.; Sciare, J.; Seland, Ø.; Shindell, D. T.; Sillman, S.; Skeie, R. B.; Spracklen, D.; Stavrakou, T.; Steenrod, S. D.; Takemura, T.; Tiitta, P.; Tilmes, S.; Tost, H.; van Noije, T.; van Zyl, P. G.; von Salzen, K.; Yu, F.; Wang, Z.; Wang, Z.; Zaveri, R. A.; Zhang, H.; Zhang, K.; Zhang, Q.; Zhang, X. The AeroCom evaluation and intercomparison of organic aerosol in global models. *Atmos. Chem. Phys.* **2014**, *14*, 10845−10895.
(144) Bond, T. C.; Doherty, S. J.; Fahey, D. W.; Forster, P. M.; Berntsen, T.; DeAngelo, B. J.; Flanner, M. G.; Ghan, S.; Kärcher, B.; Koch, D.; Kinne, S.; Kondo, Y.; Quinn, P. K.; Sarofim, M. C.; Schultz, M. G.; Schulz, M.; Venkataraman, C.; Zhang, H.; Zhang, S.; Bellouin, N.; Guttikunda, S. K.; Hopke, P. K.; Jacobson, M. Z.; Kaiser, J. W.; Klimont, Z.; Lohmann, U.; Schwarz, J. P.; Shindell, D.; Storelvmo, T.; Warren, S. G.; Zender, C. S. Bounding the role of black carbon in the climate system: A scientific assessment. *J. Geophys. Res.: Atmos.* **2013**, *118*, 5380−5552.
(145) Brune, W. H.; Miller, D. O.; Thames, A. B.; Allen, H. M.; Apel, E. C.; Blake, D. R.; Bui, T. P.; Commane, R.; Crounse, J. D.; Daube, B. C.; Diskin, G. S.; DiGangi, J. P.; Elkins, J. W.; Hall, S. R.; Hanisco, T. F.; Hannun, R. A.; Hintsa, E. J.; Hornbrook, R. S.; Kim, M. J.; McKain, K.; Moore, F. L.; Neuman, J. A.; Nicely, J. M.; Peischl, J.; Ryerson, T. B.; St. Clair, J. M.; Sweeney, C.; Teng, A. P.; Thompson, C.; Ullmann, K.; Veres, P. R.; Wennberg, P. O.; Wolfe, G. M. Exploring Oxidation in the Remote Free Troposphere: Insights From Atmospheric Tomography (ATom). *J. Geophys. Res.: Atmos.* **2020**, *125* (1), No. e2019JD031685.
(146) Wolfe, G. M.; Nicely, J. M.; St Clair, J. M.; Hanisco, T. F.; Liao, J.; Oman, L. D.; Brune, W. B.; Miller, D.; Thames, A.; Gonzalez Abad, G.; Ryerson, T. B.; Thompson, C. R.; Peischl, J.; McCain, K.; Sweeney, C.; Wennberg, P. O.; Kim, M.; Crounse, J. D.; Hall, S. R.; Ullmann, K.; Diskin, G.; Bui, P.; Chang, C.; Dean-Day, J. Mapping hydroxyl variability throughout the global remote troposphere via synthesis of airborne and satellite formaldehyde observations. *Proc. Natl. Acad. Sci. U. S. A.* **2019**, *116*, 11171−11180.

https://doi.org/10.1021/acsearthspacechem.1c00049
ACS Earth Space Chem. 2021, 5, 1436−1454